# Rates and style of Cenozoic deformation around the Gonghe Basin, northeastern Tibetan Plateau

**William H. Craddock[1,2,*], Eric Kirby[2,3,†], Huiping Zhang[4], Marin K. Clark[5], Jean-Daniel Champagnac[6], and Daoyang Yuan[7]**

[1]*U.S. Geological Survey, 12201 Sunrise Valley Drive, MS 956, Reston, Virginia 20192, USA*
[2]*Department of Geosciences, Pennsylvania State University, University Park, Pennsylvania 16802, USA*
[3]*Institute of Earth and Environmental Science, University of Potsdam, 14476 Potsdam-Golm, Germany*
[4]*State Key Laboratory of Earthquake Dynamics, Institute of Geology, China Earthquake Administration, Beijing 100029, China*
[5]*Department of Earth and Environmental Sciences, University of Michigan, Ann Arbor, Michigan 48109, USA*
[6]*Geological Institute, Swiss Federal Institute of Technology, CH-8092 Zürich, Switzerland*
[7]*Lanzhou Institute of Seismology, China Earthquake Administration, Lanzhou, Gansu 730000, China*

## ABSTRACT

The northeastern Tibetan Plateau constitutes a transitional region between the low-relief physiographic plateau to the south and the high-relief ranges of the Qilian Shan to the north. Cenozoic deformation across this margin of the plateau is associated with localized growth of fault-cored mountain ranges and associated basins. Herein, we combine detailed structural analysis of the geometry of range-bounding faults and deformation of foreland basin strata with geomorphic and exhumational records of erosion in hanging-wall ranges in order to investigate the magnitude, timing, and style of deformation along the two primary fault systems, the Qinghai Nan Shan and the Gonghe Nan Shan. Structural mapping shows that both ranges have developed above imbricate fans of listric thrust faults, which sole into décollements in the middle crust. Restoration of shortening along balanced cross sections suggests a minimum of 0.8–2.2 km and 5.1–6.9 km of shortening, respectively. Growth strata in the associated foreland basin record the onset of deformation on the two fault systems at ca. 6–10 Ma and ca. 7–10 Ma, respectively, and thus our analysis suggests late Cenozoic shortening rates of 0.2 +0.2/–0.1 km/m.y. and 0.7 +0.3/–0.2 km/m.y. along the north and south sides of Gonghe Basin. Along the Qinghai Nan Shan, these rates are similar to late Pleistocene slip rates of ~0.10 ± 0.04 mm/yr, derived from restoration and dating of a deformed alluvial-fan surface. Collectively, our results imply that deformation along both flanks of the doubly vergent Qilian Shan–Nan Shan initiated by ca. 10 Ma and that subsequent shortening has been relatively steady since that time.

## INTRODUCTION

Advances in our ability to develop precise chronologies of fault slip have increasingly led to the recognition that fault systems exhibit a wide spectrum of behavior in the way in which strain is released through time (e.g., Rockwell et al., 2000; Dragert et al., 2001). Along fault systems embedded in continental crust, variations in slip rates may reflect (1) the growth, evolution, and linkage of fault networks (e.g., Cowie et al., 1995), (2) changes in climatically modulated surface loads (e.g., Hetzel and Hampel, 2005), (3) interaction among subjacent fault strands (e.g., Oskin et al., 2008; Dolan et al., 2007), and/or (4) clustered seismicity (e.g., Rockwell et al., 2001). It is also recognized that faults embedded within deforming continental interiors may be short-lived relative to plate-boundary faults, such that they may experience periods of quiescence that extend over several to tens of millions of years (e.g., Liu et al., 2001; Bullen et al., 2003; Wang et al., 2012). Moreover, seismic hazard assessments would be greatly improved by understanding the geologic settings in which faults lacking a clear geomorphic expression of late Quaternary or Holocene displacement and/or historic earthquakes are likely to be active (e.g., Burchfiel et al., 2008; England and Jackson, 2011).

Along the northeastern margin of the Tibetan Plateau, active shortening and crustal thickening are distributed across a wide region extending from the Kunlun fault in the south to the Hexi Corridor north of the Qilian Shan (Fig. 1). Geodetic data suggest that present-day rates of shortening are ~4–6 mm/yr along a NNE cross section across this region (e.g., Zhang et al., 2004; Gan et al., 2007). High topography across this region is associated with broad sedimentary basins and E-W–trending, fault-bounded mountain ranges (Fig. 1). Although some ranges in northeastern Tibet likely experienced deformation in Eocene time (Dupont-Nivet et al., 2004; Clark et al., 2010; Duvall et al., 2011; Yuan et al., 2013), widespread exposures of Neogene–Quaternary basin fill suggest that most of these ranges are associated with thrust faults that initiated during the middle to late Miocene (Fang et al., 2005; Zheng et al., 2006; Lease et al., 2007, 2012a, 2012b; Craddock et al., 2011a; Hough et al., 2011; Zhang et al., 2012; Duvall et al., 2013; Yuan et al., 2013, and references therein). Few of these fault networks have experienced instrumental earthquakes (Global Centroid Moment Tensor Catalog, 2012); however, geomorphic observations along fault-bounded range fronts indicate that many have been active during the Holocene (Peltzer et al., 1988; Meyer et al., 1998; Van der Woerd et al., 2001; Hetzel et al., 2004; Champagnac et al., 2010; Hetzel, 2013; Zheng et al., 2013).

Current thinking about the kinematics of deformation interior to northeastern Tibet has been shaped by observations from the intracontinental strike-slip faults that bound this part of the plateau, the Kunlun and Haiyuan faults (Fig. 1). Along the Kunlun fault, a pronounced eastward decrease in left-lateral displacement rates, from >10 mm/yr across the central Kunlun to <2 mm/yr near the eastern fault terminus

*wcraddock@usgs.gov
[†]Present address: College of Earth, Ocean, and Atmospheric Sciences, Oregon State University, Corvallis, Oregon 97331, USA
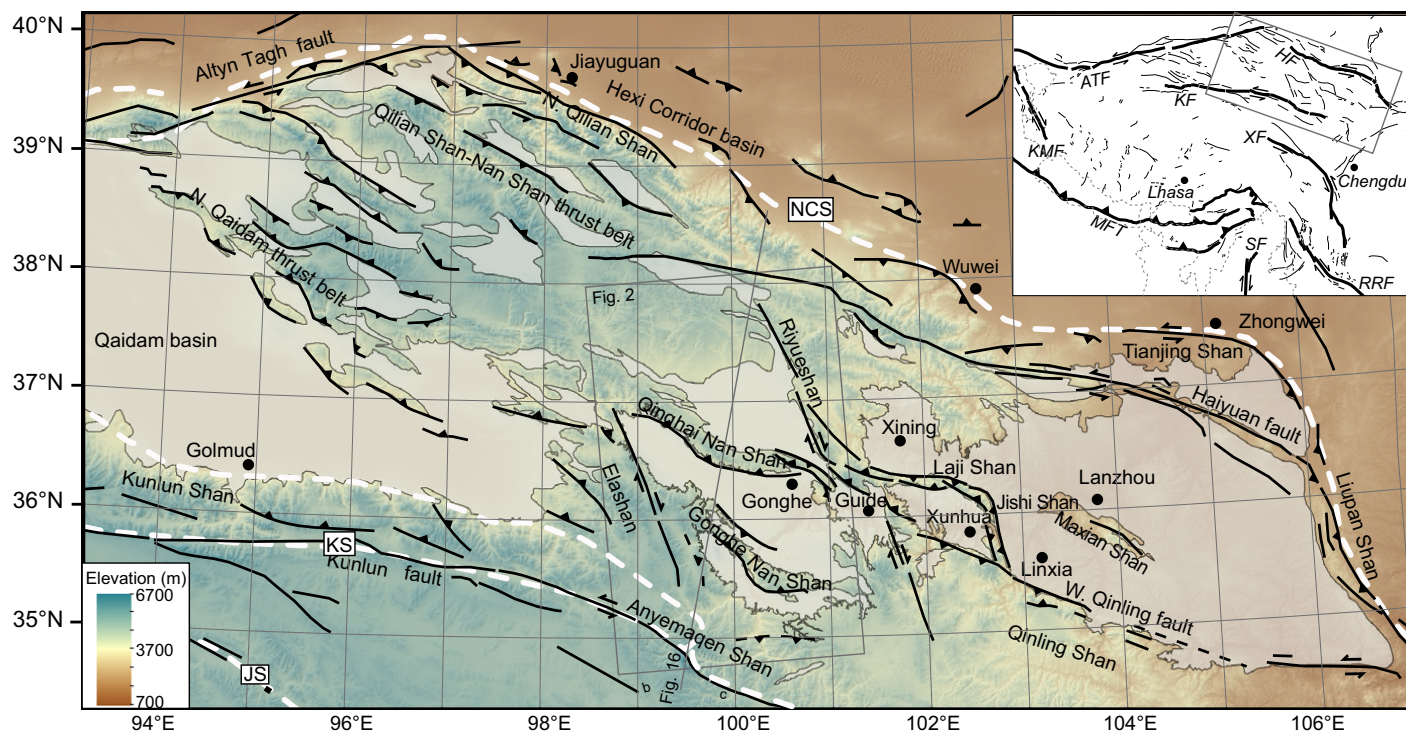
**Figure 1. Quaternary faults and Cenozoic basins (shaded) in northern Tibet. Inset also shows Quaternary faults of the Tibetan Plateau. Gray dashed lines in inset show international boundaries. Topography is GTOPO-30. Faults are adapted from Tapponnier and Molnar (1977), Molnar and Tapponnier (1978), Yin et al. (2007a), Lease et al. (2012b), Duvall et al. (2013), and Hetzel (2013). ATF—Altyn Tagh fault, HF— Haiyuan fault, KF—Kunlun fault, KMF—Karakoram fault, MFT—Main Frontal thrust fault, RRF—Red River fault, SF—Saigang fault, XF—Xianshuihe fault. White dashed lines are terrane boundaries. JS—Jinsha suture, KS—Kunlun suture, NCS—North China suture. Terrane boundaries are adapted from Yin and Harrison (2000), Yin et al. (2007b), and Pullen et al. (2008), and references therein.**

(van der Woerd et al., 2000, 2002; Kirby et al., 2007; Harkins et al., 2010), suggests that fault displacement dies out within the Tibetan Plateau. Recent studies have suggested that this slip-rate gradient may be accommodated by internal deformation within the plateau and regional clockwise rotation of the Kunlun fault (Harkins et al., 2010; Kirby and Harkins, 2013), and/or that displacement is transferred northward, across the interior of northeastern Tibet, to the Haiyuan fault (Duvall and Clark, 2010). A recent inversion of geodetic and geologic data suggests that slip along the Elashan and Riyueshan faults could indeed accommodate slip-rate gradients along the eastern Kunlun fault (Loveless and Meade, 2011), but this model requires relatively high rates of slip (~4–6 mm/yr) along these structures in order to accomplish complete transfer of slip. Geologic and geomorphic data suggest that right-lateral slip rates along the Elashan and Riyueshan faults are only ~1 mm/yr (Yuan et al., 2011), such that significant deformation must occur between the Kunlun and the Haiyuan faults on other structures in addition to the Elashan and Riyueshan faults (Duvall and Clark, 2010).

The primary focus of this manuscript is to document the rates and style of shortening along several of the primary structures likely to absorb contractional deformation between the Kunlun and the Haiyuan faults (Fig. 1). At present, rates of shortening along active thrust faults in the region are not well known. One of the most prominent structures interior to northeastern Tibet is a S-vergent thrust system associated with the Qinghai Nan Shan, which bounds the northern Gonghe Basin for ~200 km along strike (Fig. 1). Likewise, in the southern part of the basin, a second S-vergent fault network bounds the Gonghe Nan Shan (Craddock et al., 2011a) and separates the northern basin (Gonghe Basin, sensu stricto) from a southern subbasin, referred to as the Tongde subbasin (Harkins et al., 2007; Craddock et al., 2010). These two fault systems represent the primary contractional structures within northeastern Tibet between 99°E and 101°E (Fig. 1). Both fault networks terminate to the west and east against the Elashan and Riyueshan faults, and both appear to be active today. As we show, the Qinghai Nan Shan fault system is associated with a series of scarps that displace late Quaternary alluvium along its western seg-

ments, and historic earthquakes have occurred at depth beneath the Gonghe Nan Shan (e.g., Hao et al., 2012) (Fig. 2).

We address the rates and style of deformation along each of these fault systems adjacent to the Gonghe Basin complex. Following a brief geologic background, structural measurements of deformed Tertiary strata are combined with geomorphic observations in order to constrain the structural architecture of the Qinghai Nan Shan and Gonghe Nan Shan. Apatite fission-track (AFT) and apatite (U-Th)/He (AHe) cooling ages in the hanging walls are used as independent constraints on the amount of structural relief. Together, these observations provide the basis for constructing serial, deformed state cross sections through the ranges (e.g., Woodward et al., 1989). Line-length shortening measurements from restoration of deformed state cross sections combined with independent estimates of the onset of fault slip from recent studies of foreland basin stratigraphy (e.g., Craddock et al., 2011a; Zhang et al., 2012) provide the basis for determining average geologic shortening rates across the Gonghe region during the past ~5–10 m.y. We compare these long-term rates to rates

**Figure 2. Geologic map of the Gonghe Basin complex. Geology is adapted from QBGMR (1991) and field observations. Elashan and Riyueshan faults are adapted from Yuan et al. (2011) and Duvall et al. (2013).**
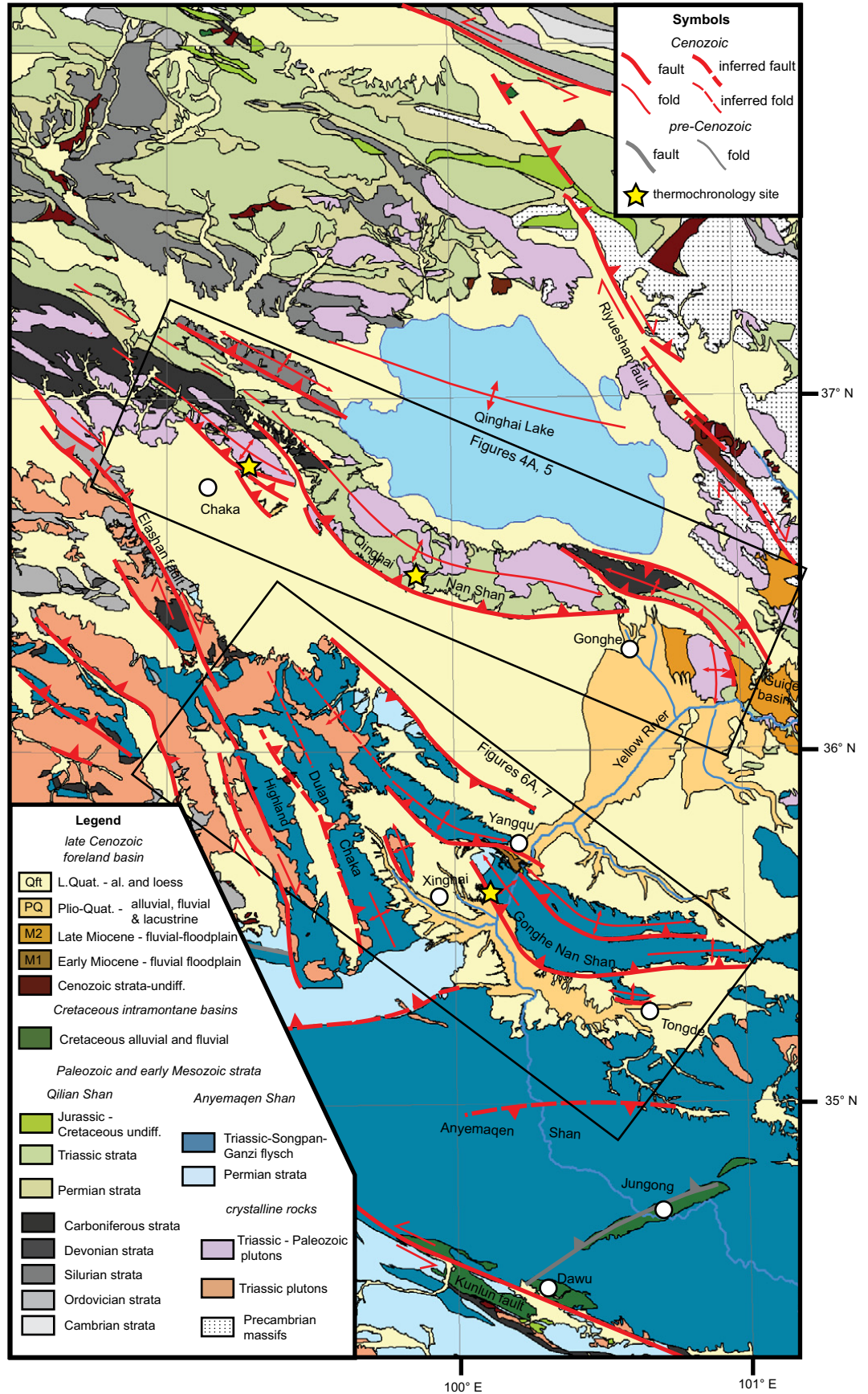
determined along the NW Qinghai Nan Shan from restoration of a displaced late Pleistocene alluvial-fan surface. Our analysis provides geologic constraints on shortening rates and style across the Qinghai Nan Shan and Gonghe Nan Shan, and our results highlight slow and perhaps steady deformation along some of the largest range-bounding fault networks interior to the northeastern Tibetan Plateau.

## GEOLOGIC SETTING

### Geology of the Qinghai Nan Shan

The Qinghai Nan Shan is one of the most prominent ranges in the interior of the northeastern Tibetan Plateau, extending E-W for ~200 km (Fig. 1). The range separates the Gonghe Basin complex to the south from Qinghai Basin to the north. The range is located along a crustal boundary separating the Paleozoic Qilian orogen from the Qaidam terrane to the south, which served as an extensional fault zone during the closure of Paleotethys Ocean in the Mesozoic (Yin et al., 2007b; Pullen et al., 2008; Zhang et al., 2014). Geologic map patterns and topography indicate that the range consists of a series of range-scale asymmetric anticlines with broad, gently dipping northern limbs, and steep, narrow southern limbs (Fig. 2). The folds are related to a network of imbricate S-vergent thrust faults. Along most of the Qinghai Nan Shan, the fault network is blind, although there are a few places where scarps in Quaternary alluvium attest to surface-breaking faults in the proximal footwall of the range. The range is cored by Paleozoic–Triassic

sedimentary rocks, reflecting a protracted history of terrane accretion in the Asian tectonic collage (Şengör and Natal'in, 1996), and the Paleozoic–Triassic strata are intruded by several phases of intermediate felsic plutons (QBGMR, 1991; Yin and Harrison, 2000; Gehrels et al., 2003; Xiao et al., 2009). Although there is evidence for widespread magmatism and pluton emplacement in the western Qilian Shan during the Paleozoic (e.g., Gehrels et al., 2003; Xiao et al., 2009), plutons in the central Qinghai Nan Shan appear to intrude rocks as young as Triassic in age (Fig. 2; QBGMR, 1991). As such, some of the plutons in the Qinghai Nan Shan appear to overlap in age with Triassic–Jurassic plutons that intrude the Songpan-Ganzi terrane to the south (QBGMR, 1991; Roger et al., 2004).

### Geology of the Gonghe Nan Shan

The Gonghe Nan Shan also extends E-W for ~200 km along strike between the Elashan and Riyueshan faults (Fig. 1). The range separates the Gonghe Basin into northern and southern subbasins, termed here the Gonghe subbasin and Tongde subbasin, respectively (Fig. 2). Similar to the Qinghai Nan Shan, the range consists of a series of asymmetric anticlines with broad, gently dipping northern limbs, and steep, narrow southern limbs (Craddock et al., 2011a). The folds are related to a network of imbricate S-vergent thrust faults that outcrop in deep exposures along the northern margin of Tongde subbasin, but that generally appear to be buried by late Quaternary alluvium. Like the Qinghai Nan Shan, the range exhibits a S-vergent topographic

asymmetry, although it appears to be more deeply eroded than its neighbor to the north. Cenozoic strata have generally been removed from the top of the range during topographic growth, and the range is cored by Triassic flysch (QBGMR, 1991).

### Sedimentary Archives of Fault Growth

Across the Gonghe region, recent magnetostratigraphic and lithostratigraphic analyses of well-exposed sedimentary sections suggest that sediment accumulation began during the early Miocene, at ca. 20 Ma (Fang et al., 2007; Craddock et al., 2011a; Lu et al., 2012). Miocene strata were generally deposited in fluvial-floodplain environments, in regions distal from source ranges. This depositional episode persisted until ca. 7–10 Ma (Craddock et al., 2011a). We refer to this early–middle Miocene stratigraphic package as M1 (Fig. 3).

The Early-Middle Miocene depocenter was disrupted during the Late Miocene by a pulse of sediment accumulation attributed to growth of ranges that define the present-day margin of the Gonghe Basin. Along the northwestern margin of the Chaka subbasin (Fig. 2), Cenozoic sediment accumulation began locally at ca. 12 Ma (Fig. 3; Zhang et al., 2012; Lu et al., 2012). The lowermost Tertiary units consist of ~700 m of muddy, fluvial and lacustrine deposits, which date to ca. 8–12 Ma (Zhang et al., 2012; Lu et al., 2012). Overlying these basal deposits is an 800-m-thick package of fluvial deposits that coarsens upward and dates to ca. 4.5–8 Ma (Zhang et al., 2012; Lu et al., 2012).

| Basin | Guide[1] | Gonghe | | | | Qaidam | |
|---|---|---|---|---|---|---|---|
| subbasin | n/a | Tongde[2] | central Gonghe[3,4] | Gonghe[4] | Chaka[5,6] | Wulan[6] | Huaitoutala[7] |
| Pleistocene | 1.8–2.6 Ma, Amigang fm. shallow lacustrine | ~3.3–0.5 Ma alluvial fan & fluvial | 0.5 Ma fluvio-lacustrine | *PQ* 0.5 Ma alluvial fan, fluvial, lacustrine | ↑ | | ≤2.5 Ma Qigequan fm. alluvial fan |
| Pliocene | 2.6–3.6 Ma, Ganjia fm. alluvial fan | | >3.8 Ma | | <4.5 Ma alluvial fan | | 2.5–8.1Ma Shizigou fm. fluvial-floodplain |
| | 3.6–>7.0 Ma, Herjia fm. braided river | ↓ | ↓ | *M2* ~3.3–6 Ma fluvial-floodplain | ~4.5–8 Ma fluvial-floodplain | | |
| Miocene | >7.0–>12 Ma, Ashigong fm. braided river | | | 11–9 Ma | ~8–12 Ma fluvio-lacustrine | ~9 Ma fluvial and lacustrine | 8.1–15.3 Ma Shang Youshashan fm. fluvial-floodplain |
| | <16–19 Ma Garang fm. fluvial | | | *M1* fluvial-floodplain 21 Ma | | | 15.3–15.8 Ma Xia Youshashan fm. fluvial-floodplain |
| | 19–20.8 Ma, Guidemen fm. alluvial fan | | | | | ~22 Ma | |
| Oligocene | Xining Gp. | | | | | | |

Figure 3. Existing constraints on the age of the Cenozoic basin fill in the Gonghe Basin complex, and a comparison to the stratigraphic units in Guide Basin and northeastern Qaidam Basin, adapted from Fang et al. (2005, 2007). Units are color coded according to our regional lithostratigraphic correlation. Lithostratigraphic units used in this study are labeled in the Gonghe subbasin stratigraphic column. 1—Fang et al. (2005); 2—Craddock et al. (2010); 3—Zheng et al. (1985); 4—Craddock et al. (2011a); 5—Zhang et al. (2011); 6—Lu et al. (2012); 7—Fang et al. (2007). Arrows indicate that top or bottom of section is either not exposed or not measured.

Similar facies associations are observed in sections adjacent to the Gonghe Nan Shan (Craddock et al., 2011a), and collectively we refer to these upper Miocene fluvial sequences as M2 (Fig. 3).

Around the margins of the Gonghe Basin complex, the uppermost strata consist of coarse-grained fluvial conglomerates that prograde into the basin. In the Chaka subbasin (e.g., Zhang et al., 2012), this upper package is >300 m of alluvial-fan deposits that range in age from ca. 4.5 Ma to less than 3.0 Ma. On the flanks of the Gonghe Nan Shan (Craddock et al., 2011a), the uppermost ~500 m of section consists of coarse alluvial-fan and fluvial conglomerates, some of which are associated with the axial Yellow River, and these strata date to ca. 7–0.5 Ma (Craddock et al., 2010, 2011a). Gravels along the basin margins generally grade laterally into finer-grained sands and muds, interpreted to be fluvial, and perhaps lacustrine, deposits (Craddock et al., 2010, 2011a). We refer to the various Pliocene–Quaternary gravels and sands as PQ (Fig. 3), and the abbreviations PQal and PQfl distinguish between Pliocene–Quaternary strata that we interpret to be deposited in an alluvial-fan (al) or fluvial (fl) environment, respectively.

A combination of stratigraphic and structural observations brackets the timing of shortening along the NW Qinghai Nan Shan, along the northern margin of the Chaka Basin, to the past ~6 m.y. (Zhang et al., 2012). In addition to the coarsening-upward sequence in the upper half of the basin fill, a pronounced drainage reversal occurs in this upper stratigraphic package, from N-flowing to S-flowing paleocurrents. Moreover, this reversal corresponds to fanning dips that are interpreted as growth strata in the proximal footwall of the Qinghai Nan Shan thrust fault network (Zhang et al., 2012).

In the Gonghe Nan Shan, similar changes attest to the onset of fault activity and range growth between 7 and 10 Ma (Craddock et al., 2011a). The lower stratigraphic packages (M1 and M2) in southern Gonghe Basin are truncated by a prominent unconformity, which is overlain by the ~500 m of conglomerate that dates to ca. 7–0.5 Ma (Craddock et al., 2010, 2011a). The conglomerate succession is interpreted to be coalesced alluvial-fan deposits that were shed off high topography around the basin margins. Along both the southern and northern flanks of the Gonghe Nan Shan, alluvial-fan deposits exhibit growth strata and progressive unconformities, indicating that growth of the range and fault activity in the Gonghe Nan Shan initiated between 7 and 10 Ma (Craddock et al., 2011a) and persisted during accumulation of alluvial-fan strata on the flanks of the range.

Regionally, the onset of shortening along the Qinghai Nan Shan and Gonghe Nan Shan is similar to the onset of right-lateral strike-slip faulting along the eastern and western basin margins (Fig. 1). Slip rates along the Elashan fault determined from displaced Pleistocene alluvium yield values of 1.1 ± 0.3 mm/yr (Yuan et al., 2011); assuming constant slip through time, finite displacement of ~9–15 km from piercing points in pre-Cenozoic bedrock suggests that fault initiation occurred ca. 9 ± 3 Ma (Yuan et al., 2011; Lu et al., 2012). This estimate is similar to, albeit slightly younger than, an acceleration in mineral cooling rates in the hanging walls of two reverse fault–bounded ranges to the SW of the Elashan fault, in the Dulan-Chaka highland (Fig. 2), from 17 to 12 Ma (Duvall et al., 2013). Combined Pleistocene slip rates and offset piercing points along the Riyueshan fault, at the eastern terminus of the Qinghai Nan Shan, suggest that this structure also initiated around 9 ± 3 Ma (Yuan et al., 2011). All of these estimates are similar to the 10 ± 3 Ma initiation inferred for contractional structures along the northwestern margin of Guide Basin (Fig. 1; Fang et al., 2005; Lease et al., 2007; Yuan et al., 2011). In summary, geologic data consistently show that the initiation of shortening and strike-slip faulting in this part of northeastern Tibet occurred at ca. 7–12 Ma, and likely a few million years earlier in the Dulan-Chaka highlands to the west.

## FAULT SYSTEM ARCHITECTURE

### Structural Geology along the Qinghai Nan Shan

We conducted detailed structural mapping at several locations along the Qinghai Nan Shan range front (Fig. 4). Generally, Cenozoic strata are steeply dipping along the range front and dip angles decrease toward the basin, where strata are nearly horizontal. Faults in the proximal footwall of the NW Qinghai Nan Shan in the Chaka region provide excellent exposure of foreland basin strata, which we exploit for two structural transects (Fig. 4B; also see Zhang et al., 2012). Along the eastern transect, the basal M2 and PQfl strata dip 30°SW but are folded into a narrow, ~1-km-wide syncline near the range front. Along the western transect, the correlative beds dip steeply, ~50°–60° to the SW, and they are folded into a small anticline that sits above a bedrock sill near the range front. Basal deposits grade up section into a >1-km-thick package of PQ sandstones and gravels. Along the eastern structural transect, bedding dips in the mid- to upper levels of PQ progressively decrease up section, such that

the highest exposed PQal strata are nearly flat-lying (Fig. 4).

A second exposure of continuous section exists within the Yellow River canyon along the flanks of the far eastern Qinghai Nan Shan near Gonghe City (Fig. 4). In a tributary canyon NNW of Gonghe City (Fig. 4), PQ gravels are in unconformable contact with the bedrock core of the Qinghai Nan Shan, and dip 45°S. Hundreds of meters to the south, the PQal strata are flat-lying. Fanning dips in PQ strata along the eastern Qinghai Nan Shan front provide a hint that the local timing of thrusting may be similar to what has been documented at Chaka (Zhang et al., 2012) and in northwest Guide Basin (Fang et al., 2005; Lease et al., 2007). However, fanning dips at this locality may also reflect a fold hinge, hundreds of meters wide, in the proximal footwall of the range. If so, fold growth would have postdated PQ deposition locally. We favor the former interpretation but acknowledge that the timing is somewhat equivocal.

Late Cenozoic strata are also well exposed on the flanks of granitic bedrock that outcrops ~20 km east of Gonghe City (Fig. 4C). The range is bound by a NE-vergent thrust fault along its eastern edge, which dips ~60°W. Notably, the vergence of the fault bounding this subrange opposes the vergence of faults bounding much of the Qinghai Nan Shan to the west. Along the west side of the small range east of Gonghe City, M2 strata onlap the granitic bedrock and dip gently, ~5°–10°W, suggesting that, like the broader Qinghai Nan Shan, this small subrange near Chaka exhibits a pronounced asymmetry, with a faulted eastern flank and a broad, slightly tilted western flank. Although M2 strata dip 20°–50°E in several outcrops in the proximal footwall of the fault, M2 dip decreases to 6°–10°E within a few kilometers to the east (Fig. 4C). Notably, in one ~80-m-thick exposure, dig angles in E-dipping strata progressively decrease up section. Near the top of the outcrop, beds dipping ~31°SE are truncated by 22°SE-dipping beds immediately above (field photographs in the Supplemental File[1]).
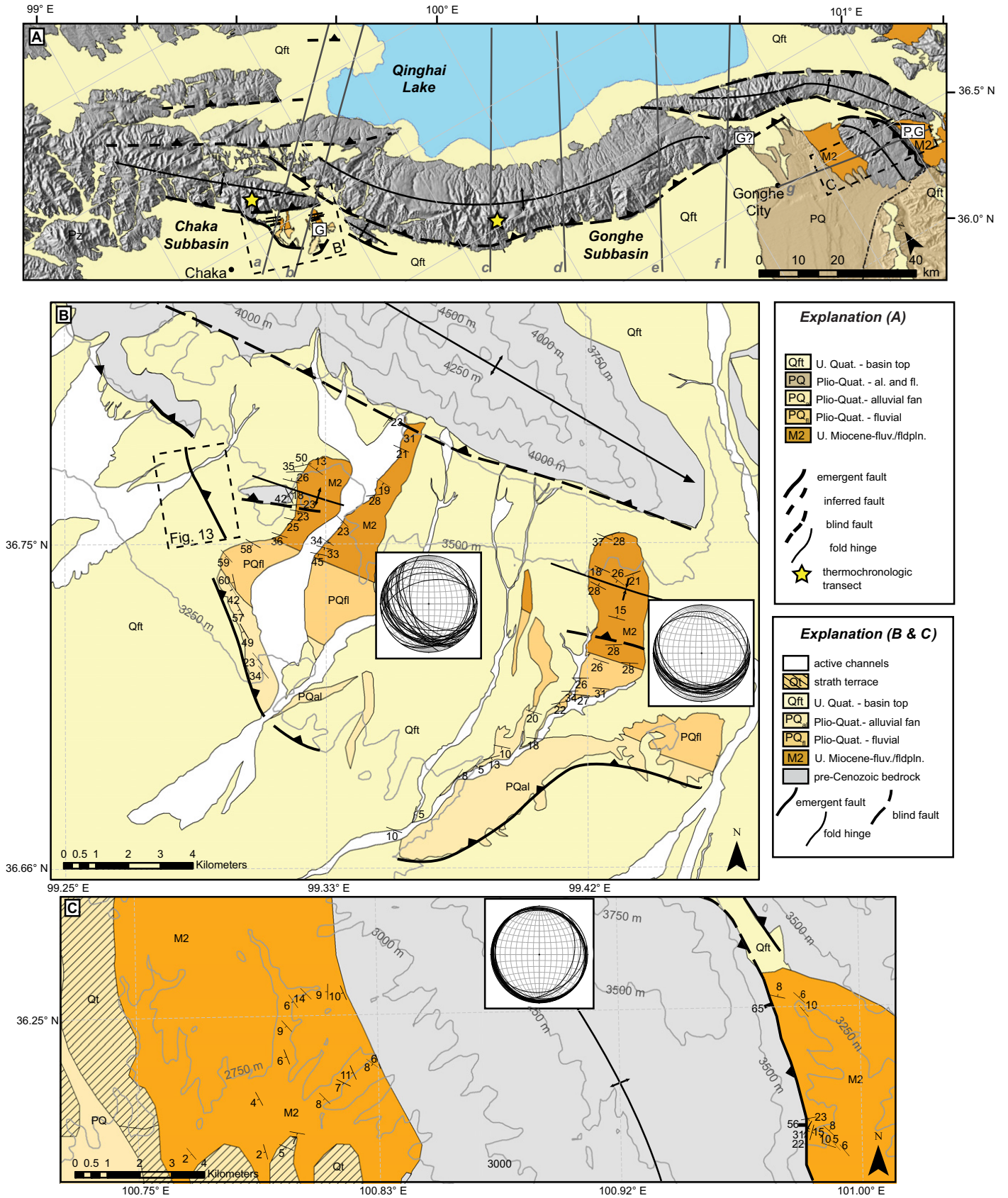
Figure 4. (A) Geology of the northern Gonghe Basin complex, including detailed maps of western (B) and eastern (C) Qinghai Nan Shan range front. Cross sections A–G are shown in Figure 11. Sites are labeled. P—progressive unconformity; G—growth strata.

This progressive unconformity and associated fanning dips on the eastern side of the pluton indicate that the fault along the eastern edge of the pluton was likely active during M2 deposition. Similar growth strata are associated with mesoscale faults that cut M2 strata nearby (additional photograph in the Supplemental File [see footnote 1]). Although these deposits have not been dated directly, they appear to be correlative with 3.6–7.0 Ma Herjia Formation strata in the Guide Basin to the east (Fig. 3; Fang et al., 2005). Provided that our lithostratigraphic correlation is accurate, it would augment evidence for synchronous shortening along the strike of the Qinghai Nan Shan.

## Topographic and Geophysical Constraints on Qinghai Nan Shan Architecture

Although Cenozoic strata are not preserved along the crest of the Qinghai Nan Shan, the topography of the range appears to contain information about its structural architecture. The southern limb of the range, which is flanked by the steeply S-dipping strata described already, exhibits steep, highly dissected topography (Fig. 5). Local topographic relief (i.e., maximum elevation–minimum elevation) within a 1-km-radius circular window exceeds 1000 m. In contrast, the northern limb of the range dips N at a very low angle (generally 3°–5°), and topographic relief along this surface is generally

<100 m. We interpret the broad, flat, slightly N-dipping surface along the northern side of the Qinghai Nan Shan to be a relict erosion surface that represents a paleohorizontal structural marker and predates growth of the S-vergent anticline that cores the range, making it a key constraint on the structural relief of the Qinghai Nan Shan.

Recent seismic-reflection surveys reveal the architecture of the deeper levels of the basin fill to the north of the Qinghai Nan Shan (An et al., 2006). The surveys show ~500–1000 m of sediment in Qinghai Basin. The deep strata dip at a low angle to the north across the southern part of the basin, and the pattern suggests that the northern limb of the range extends far to the
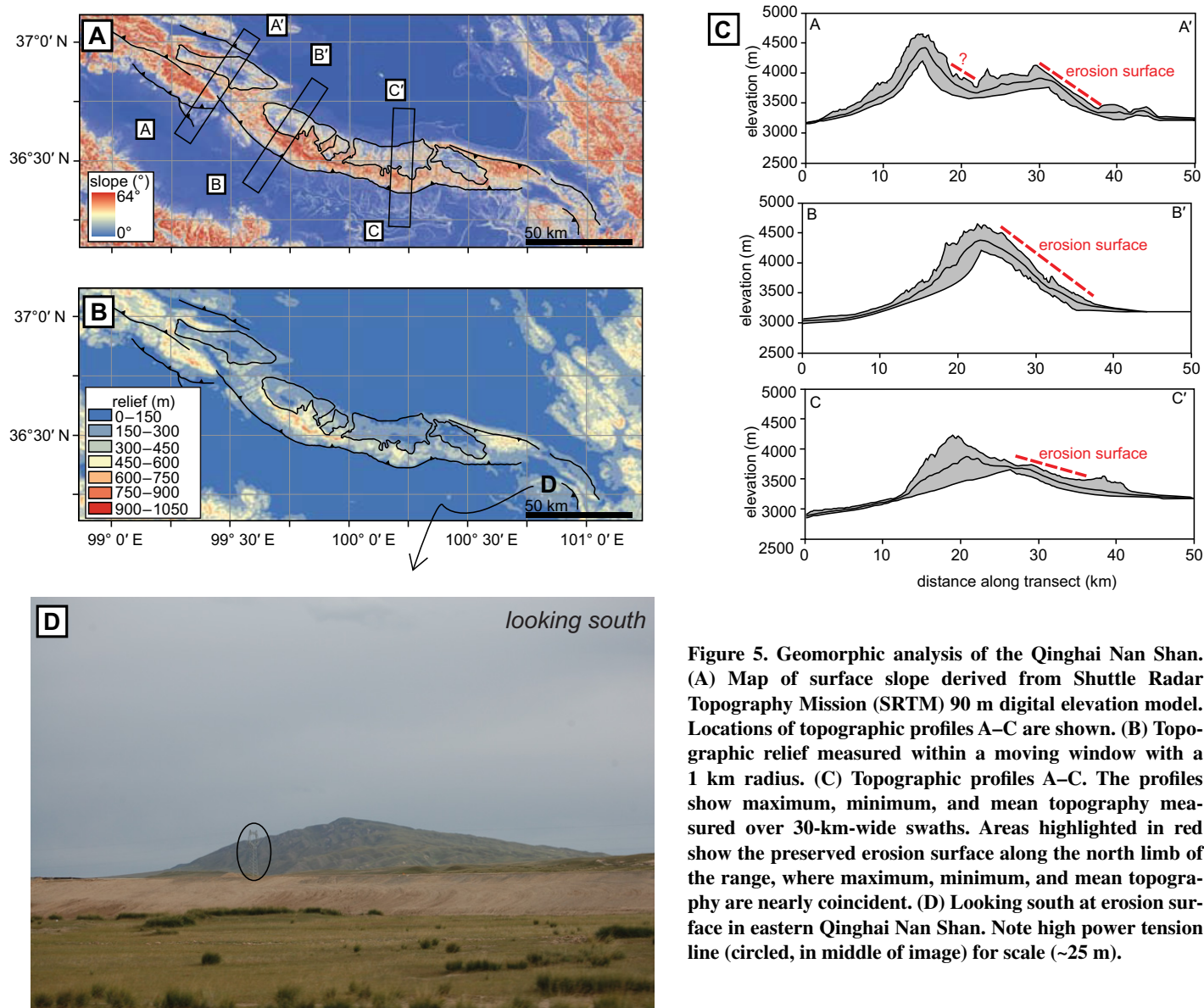


Figure 5. Geomorphic analysis of the Qinghai Nan Shan. (A) Map of surface slope derived from Shuttle Radar Topography Mission (SRTM) 90 m digital elevation model. Locations of topographic profiles A–C are shown. (B) Topographic relief measured within a moving window with a 1 km radius. (C) Topographic profiles A–C. The profiles show maximum, minimum, and mean topography measured over 30-km-wide swaths. Areas highlighted in red show the preserved erosion surface along the north limb of the range, where maximum, minimum, and mean topography are nearly coincident. (D) Looking south at erosion surface in eastern Qinghai Nan Shan. Note high power tension line (circled, in middle of image) for scale (~25 m).

north, beneath the Qinghai Basin. Similarity in dip between the strata in the southern Qinghai Lake basin and the low-relief, gently dipping topographic surface on the northern limb of the Qinghai Nan Shan range bolsters evidence that the northern limb of the Qinghai Nan Shan was once a flat-lying erosion surface. Seismic-reflection profiles in the Qinghai Lake basin also suggest the presence of a minor approximately WNW-striking structural high below the central portion of the basin (Fig. 2; An et al., 2006).

### Structural Geology across the Gonghe Nan Shan

We also conducted detailed structural mapping across the Gonghe Nan Shan, where the Yellow River cuts an ~700-m-deep canyon across the range (Fig. 6). In general, our mapping reveals a broad, range-scale anticline at the western tip of the eastern subrange, which appears to verge to the SSW and plunges gently to the WNW (Fig. 6). Along the southern range front, the range-bounding fault is exposed and places bedrock over discontinuous exposures of M1 strata along the southern range front (see Fig. 3). The M1 red beds are overturned and dip ~30°ENE. Along the Yellow River canyon, PQ conglomerate beds are in unconformable contact with the highly deformed metasedimentary rocks that core the Gonghe Nan Shan, and dip angles progressively decrease up section toward the top of the basin fill; beds are subvertical just above the basal unconformity, and they are subhorizontal at the basin surface. Moreover, in this outcrop, PQ exhibits prominent intraformational unconformities, which can be traced into correlative conformities only a few hundred meters to the south. The progressive tilting and intraformational unconformities in PQ strata indicate that the unit accumulated during fault slip (see Craddock et al., 2011a). Farther south, PQ strata are subhorizontal across the interior of Tongde subbasin.

In the canyon on the north side of the range, mapping along multiple structural transects indicates that both M1 and M2 are folded into a 20°–30°NNE-dipping panel (Fig. 6). In contrast to the relatively uniform dips in the lower part of the section, PQ strata exhibit relatively low dips in this region, ranging from ~0° to 15°. Immediately north of the small village of Yangqu (Fig. 6), an ~450-m-thick exposure of PQ gravels is well exposed along the western canyon wall. Bedding dips in this outcrop progressively decrease upward from ~10°–15°NE at the base of the section to subhorizontal at the top (details can be found in Craddock et al., 2011a). Furthermore, unit PQ in this region is in angular unconformable contact with the under-

lying M1 and M2 deposits, and the degree of angular discordance diminishes toward the north, away from the range and from the axis of the anticline. Similar to the southern Gonghe Nan Shan front, decreases in dip of the PQ strata up section and variable degrees of angular discordance both imply tilting of the Gonghe Nan Shan during PQ deposition, which is attributed to deformation in the synformal hinge along the back limb of the Gonghe Nan Shan fault-fold system. To the north, PQ strata are generally flat-lying in the Yellow River canyon.

A few kilometers to the south of the village of Yangqu, M1 and M2 strata define an anticline that plunges at a low angle to the west (Fig. 6). The fold is several kilometers wide, and it appears to extend to the SE into the range, although the Neogene strata that define the architecture of this fold have been eroded. The structural high in the core of this fold projects along strike into the topographic high to the north of a saddle interior to the range, and the structural low along the southern front of the fold projects along strike into the topographic saddle that is interior to the Gonghe Nan Shan. Because of the correspondence between structural relief near the village of Yangqu and elevation of the Gonghe Nan Shan along strike to the east, we interpret that the topographic saddle interior to the Gonghe Nan Shan delineates a range-scale structural low, and that the eastern Gonghe Nan Shan consists of two imbricated thrust sheets. In support of this interpretation, remnants of M1 or M2 strata (see Fig. 3; see also QBGMR, 1991) are preserved in the structural saddle in the middle of the range, indicating that the topographic low is also a structural low, which must extend at least several tens of kilometers to the SE of the town of Yangqu.

Near the small village of Jiala, the fault that bounds the western subrange is well exposed and dips 27°N (Fig. 6). North of Jiala, the western range is covered by basin fill, but ~10 km to the east, the eastern terminus of the range outcrops in the deepest part of the Yellow River canyon. At both sites, PQ deposits bury the western subrange, indicating that range growth predated PQ deposition locally.

A narrow bedrock sill outcrops just north of the Gonghe Nan Shan range, and finely laminated silts associated with PQ strata are tilted up to 20° along the flank of this structure (Fig. 6), indicating that deformation persisted into late Pleistocene time. We consider this sill to be related to an ~NNE-vergent back thrust to the Gonghe Nan Shan (Fig. 4). The primary evidence for this comes from a $M_w$ 6.4 earthquake beneath Gonghe Basin, on 26 April 1990 (e.g., Hao et al., 2012, and references therein). Inversions of line-leveling data suggest that the event

occurred on a NNE-vergent fault plane located in the southern part of Gonghe Basin, the surface projection of which would lie 10–20 km to the north of the bedrock sill (see Chen et al., 1996; Chen and Xu, 2000; Hao et al., 2012).

On the SW margin of Tongde subbasin, an angular unconformity separates NNE-dipping M2 strata from flat-lying PQ strata (Fig. 6; Supplemental File [see footnote 1]), suggesting that the range along the southern margin of Tongde subbasin may have been active at a similar time as the Gonghe Nan Shan.

### Topographic Constraints on Gonghe Nan Shan Fault Geometry

In contrast to the Qinghai Nan Shan, both the northern and southern flanks of the Gonghe Nan Shan are characterized by steep slopes and relatively high local relief compared to the Qinghai Nan Shan (Fig. 7). Nevertheless, the topography of the range is also asymmetric from north to south, particularly along serial topographic profiles; relief measured within a 1 km window is generally relatively low on the northern side of the range; and relict, N-dipping erosion surfaces can be seen around the region at lower elevations (Fig. 7). The ranges to the south and west of the Gonghe Nan Shan (Fig. 1) also appear to exhibit S-vergent topographic asymmetry, similar to the Gonghe Nan Shan, and, we argue by analogy that the southern ranges are also likely related to S-vergent thrust faults. The E-W–striking topographic saddle that divides the eastern half into two subranges, and projects along strike into the synclinal hinge south of the village of Yangqu (Fig. 6), is generally ~500 m lower than adjacent peaks to the north and south and extends along strike across much of the eastern Gonghe Nan Shan (Fig. 7).

### LOW-TEMPERATURE THERMOCHRONOLOGY

The cooling history of hanging-wall blocks can be used to place bounds on the timing of fault slip (e.g., Erdős et al., 2014), if exhumation is deep enough to drive cooling of >~50 °C (for apatite helium dating; Reiners and Brandon, 2006), or, if exhumation is minimal, samples that resided above their closure temperature when faulting began may represent a relict thermal stratigraphy that can passively record hanging-wall motion (e.g., McPhillips and Brandon, 2010; Clark et al., 2010). To determine the exhumation histories of hanging-wall ranges, we collected low-temperature thermochronologic samples along vertical transects on the southern flanks of the Qinghai Nan Shan and the Gonghe Nan Shan (Fig. 8; Table 1).
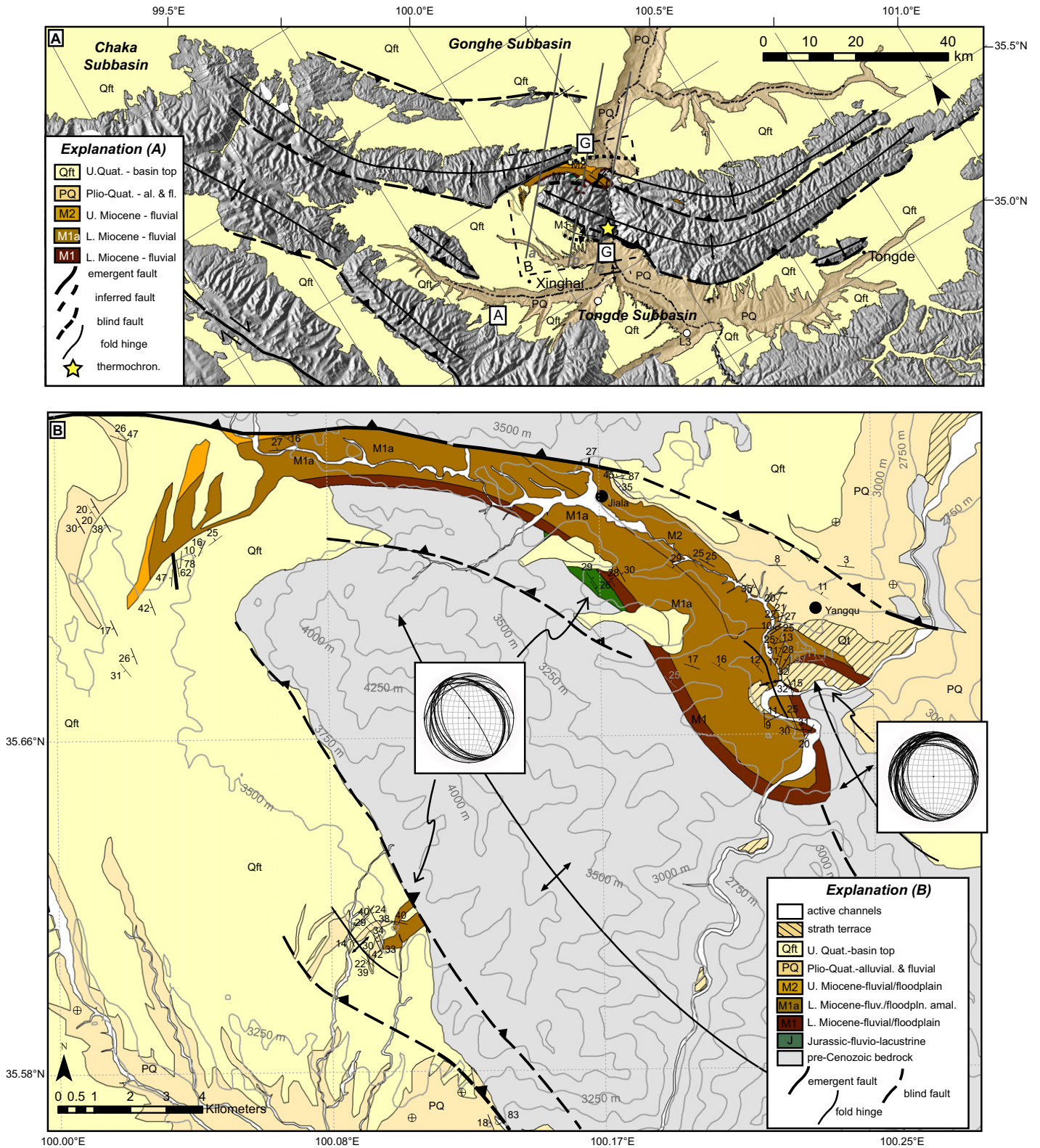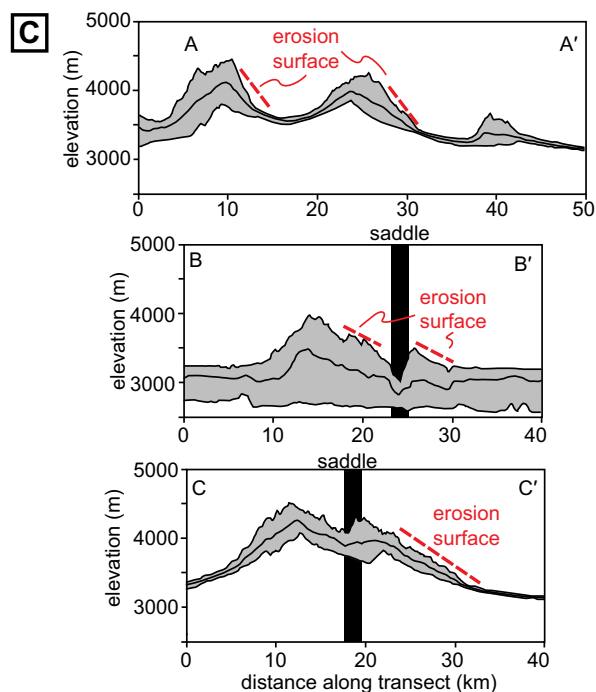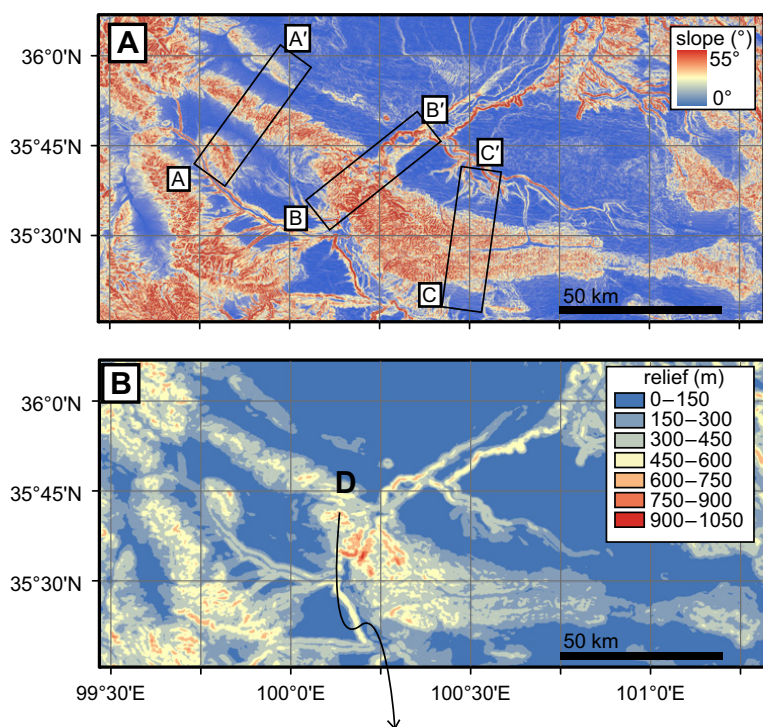
**Figure 6. Geology of the southern Gonghe Basin complex, including a detailed map of the Yellow River canyon where it crosses the Gonghe Nan Shan. Sites labeled G exhibit progressive unconformities and growth strata, and site labeled A exhibits an angular unconformity between NNE-dipping M2 and flat-lying PQ. Cross sections a, b, and c are shown in Figure 12.**

Figure 7. Geomorphic analysis of the Gonghe Nan Shan. (A) Map of surface slope derived from Shuttle Radar Topography Mission (SRTM) 90 m digital elevation model. Locations of topographic profiles A–C are shown. (B) Topographic relief measured within a moving window with a 1 km radius. (C) Topographic profiles A–C. The profiles show maximum, minimum, and mean topography measured over 30-km-wide swaths. The vertical black bars in sections B-B′ and C-C′ show the location of the prominent topographic break in the central part of the range. (D) Looking east at the Gonghe Nan Shan erosion surface. Note high power tension line (middle of image) for scale (~25 m).

The Qinghai Nan Shan transect is located in the central part of the range (sample locations shown in Figs. 2 and 4; Table 1), and two additional samples were collected in the vicinity of the Chaka structural transect, in the western Qinghai Nan Shan. The sample locations were chosen in part because they correspond to some of the only exposures of plutonic rock in the range with high potential for yielding grains suitable for apatite (U-Th)/He thermochronology. The two western Qinghai Nan Shan samples have the additional benefit of being adjacent to the previously described structural mapping and magnetostratigraphic section (Zhang et al., 2012), and they allow us to test the consistency of the vertical transect

along strike of the Qinghai Nan Shan range. The central Qinghai Nan Shan transect (~1 km relief) spans the highest-relief part the range, where potential for observing cooling related to late Cenozoic range growth is highest (Figs. 2 and 8; Table 1).
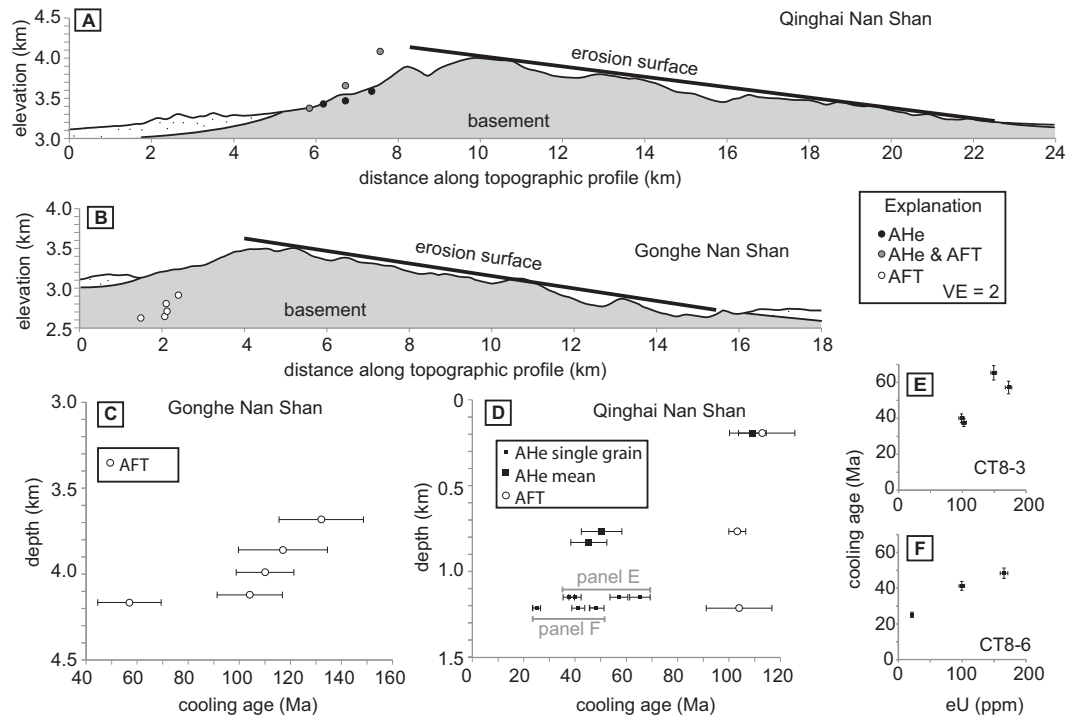
The vertical transect on the south side of the Gonghe Nan Shan is located near our structural mapping site in the Yellow River canyon, in the proximal hanging wall of the range-bounding fault (Figs. 2, 6, and 8; Table 1). We sampled sandstone beds in the Triassic Songpan-Ganzi flysch that cores the range because plutonic rocks are not mapped in the central part of the range (QBGMR, 1991). This vertical transect spans only ~0.4 km of relief, although it appears

to represent the deepest Neogene structural levels in the range.

Apatites were separated from rock samples using standard mineral separation techniques. Using optical microscopes at the University of Michigan and the California Institute of Technology, we selected at least two grains, and up to five grains, from the Qinghai Nan Shan samples. We selected grains exhibiting equant, euhedral geometry, and a lack of visible birefringent inclusions. Apatite (U-Th)/He (hereafter referred to as AHe) cooling ages were measured at the California Institute of Technology following the methods in Farley (2002) (Table 2). Cooling ages were measured for a few grains with radius ($r$) < 36 μm, which pro-

**Figure 8. Geologic setting of apatite fission-track (AFT) and (U-Th)/He samples (AHe). (A) Central Qinghai Nan Shan vertical transect; 90 m Shuttle Radar Topography Mission elevation data and samples projected onto a profile orthogonal to range front. (B) Gonghe Nan Shan vertical transect. Topographic profile measured perpendicular to range front, ~7 km NW of samples, which were collected in the Yellow River canyon, in order to show relationship between samples and erosion surface. (C) Cooling age vs. structural depth for Gonghe Nan Shan AFT samples. (D) Cooling age vs. structural depth for Qinghai Nan Shan AHe and AFT samples. Uncertainties on mean cooling ages are two standard errors, calculated from the standard deviation of**



**replicate cooling ages for a single sample. Due to cooling age–eU correlation, no mean ages are reported from samples CT8–3 and CT8–6, at elevations of 3567 m and 3500 m, respectively. Rather, for these grains, all single-grain cooling ages are reported. Uncertainties are two standard deviations based on the reproducibility of Durango apatite. (E–F) AHe cooling age vs. eU concentration for lowest two samples from central Qinghai Nan Shan vertical transect. Two standard deviation uncertainties on eU reflect analytical uncertainties, and two standard deviation uncertainties on single-grain cooling ages reflect Durango apatite cooling age reproducibility. Grains with radii <36 μm are not shown.**

duced large age scatter for replicate analyses from single samples (Farley, 2002). Although analytical work was conducted for a few grains with $r$ < 36 μm, we excluded these from interpretations because the alpha-ejection correction represents a large fraction of the corrected age (Farley, 2002). Apatites from flysch samples were, in contrast, generally smaller, and broken and frosted, and they were considered unsuitable for (U-Th)/He thermochronology. Single-grain AHe ages are reported, and we ascribe two standard deviation uncertainties of 6% for single-grain analyses, based on the standard deviation of Durango apatite, which exceeds that of the propagated analytical uncertainties (Table 2; Farley, 2002).

In total, three of eight samples (CT8–4, CT8–2, and CT8–22) yielded reproducible single-grain cooling ages. For these three samples, we report mean ages and two standard error uncertainties, which are based on the standard deviation of cooling ages from each of the individual samples. Two additional samples (CT8–6 and CT8–3) at the lowest elevation along the central Qinghai Nan Shan transect exhibited strong cooling age versus effective uranium (hereafter, eU) concentration correlations (see Shuster et al., 2006; Flowers et al., 2009; see

Figs. 8E and 8F). Effective uranium is a proxy for radiation damage, which affects the closure temperature of the apatite (U-Th)/He system, the effect of which can be enhanced at slow cooling rates (<~4 °C/m.y.), such that samples with age-eU correlations essentially serve as

multiple thermochronometers and enable particularly well-constrained inverse modeling of time-temperature history (Flowers et al., 2009). For these two samples, we display single-grain cooling ages on the age-elevation plot (Fig. 8D), with two standard deviation uncertainties

### TABLE 1. THERMOCHRONOLOGIC SAMPLES

| | Location | | | | | | |
| Sample | Latitude (°N) | Longitude (°E) | Elevation (m) | Mean AHe age (Ma) | AHe 2SE (Ma) | AFT age* | AFT 2SE (Ma) |
|---|---|---|---|---|---|---|---|
| Central Gonghe Nan Shan | | | | | | | |
| CT9-5 | 35.57081 | 100.16589 | 3055 | – | – | 132.0 | 16.5 |
| CT9-4 | 35.56894 | 100.16531 | 2914 | – | – | 117.0 | 17.4 |
| CT9-3 | 35.56703 | 100.16817 | 2785 | – | – | 110.0 | 11.3 |
| CT9-2 | 35.56556 | 100.16836 | 2699 | – | – | 104.0 | 12.8 |
| CT9-1 | 35.56381 | 100.16317 | 2672 | – | – | 56.9 | 12.4 |
| Central Qinghai Nan Shan | | | | | | | |
| CT8-4 | 36.51795 | 99.85350 | 4443 | 109.2 | 5.4 | 113 | 12.7 |
| CT8-2 | 36.50339 | 99.87925 | 3875 | 50.5 | 7.9 | 103.3† | 3.3 |
| CT8-22 | 36.51173 | 99.87052 | 3782 | 45.5 | 7.0 | – | – |
| CT8-24 | 36.50562 | 99.87278 | 3624 | NA§ | – | – | – |
| CT8-3 | 36.50080 | 99.87118 | 3567 | NA# | – | – | – |
| CT8-6 | 36.49718 | 99.87175 | 3500 | NA# | – | 104.0 | 12.8 |
| Western Qinghai Nan Shan | | | | | | | |
| CT8-7 | 36.85596 | 99.25148 | 4410 | – | – | – | – |
| CT8-19 | 36.82912 | 99.25431 | 3700 | 194.1 | 122.9 | – | – |

*Note:* 2SE—two standard error. AHe—(U-Th)/He.
*Pooled age is reported for apatite fission-track (AFT) data.
†AFT central age.
§No mean ages reported for samples with 0–1 single-grain ages.
#No mean age reported because of correlation between eU and cooling ages.

TABLE 2. APATITE (U-Th)/He DATA

| Replicate | U (ppm) | Th (ppm) | eU (ppm) | He (nmol/g) | Mass (µg) | Ft* | Radius (µm) | Length (µm) | Raw age (Ma) | Corr. age (Ma) | Uncertainty[†] (Ma) |
|---|---|---|---|---|---|---|---|---|---|---|---|
| Central Qinghai Nan Shan | | | | | | | | | | | |
| CT8-4 | | | | | | | | | | | |
| a | 175.5 | 128.8 | 205.8 | 78.7 | 1.5 | 0.61 | 36 | 166 | 69.9 | 114.9 | 6.9 |
| b | 100.2 | 46.7 | 111.2 | 44.2 | 1.7 | 0.65 | 40 | 160 | 72.6 | 111.9 | 6.7 |
| c | 125.6 | 100.4 | 149.2 | 66.1 | 2.9 | 0.75 | 58 | 177 | 80.9 | 107.4 | 6.4 |
| d | 87.1 | 48.2 | 98.4 | 41.8 | 1.7 | 0.76 | 58 | 120 | 77.5 | 102.6 | 6.2 |
| | | | | | | | | | mean[§]: | **109.2** | **5.4** |
| CT8-2 | | | | | | | | | | | |
| a | 113.6 | 35.3 | 121.8 | 27.4 | 2.2 | 0.76 | 59 | 141 | 41.2 | 54.2 | 3.3 |
| b | 99.5 | 29.9 | 106.6 | 24.7 | 2.0 | 0.77 | 62 | 133 | 42.3 | 54.8 | 3.2 |
| c | 104.9 | 23.1 | 110.3 | 18.4 | 1.7 | 0.72 | 50 | 122 | 30.6 | 42.6 | 2.5 |
| | | | | | | | | | mean[§]: | **50.5** | **7.9** |
| CT8-22 | | | | | | | | | | | |
| a | 122.8 | 14.9 | 126.3 | 17.4 | 2.1 | 0.71 | 48 | 136 | 25.3 | 35.7 | 2.1 |
| b | 75.4 | 17.5 | 79.6 | 14.0 | 1.3 | 0.71 | 49 | 115 | 32.2 | 45.2 | 2.7 |
| c | 110.7 | 9.6 | 112.9 | 20.3 | 1.3 | 0.67 | 42 | 118 | 32.9 | 49.2 | 3.0 |
| d | 74.2 | 21.5 | 79.3 | 15.1 | 1.2 | 0.67 | 43 | 113 | 34.8 | 51.7 | 3.1 |
| | | | | | | | | | mean[§]: | **45.5** | **7.0** |
| CT8-24 | | | | | | | | | | | |
| a[#] | 10.1 | 30.2 | 17.2 | 2.8 | 0.8 | 0.57 | 34 | 106 | 29.4 | 51.8 | 3.2 |
| b | 73.7 | 50.4 | 85.6 | 30.4 | 0.7 | 0.64 | 39 | 91 | 64.9 | 101.8 | 6.1 |
| | | | | | | | | | mean: | n/a** | |
| CT8-3 | | | | | | | | | | | |
| a | 162.7 | 43.0 | 172.8 | 34.2 | 1.1 | 0.63 | 38 | 121 | 36.2 | 57.2 | 3.5 |
| b[#] | 154.8 | 21.5 | 159.8 | 28.3 | 0.7 | 0.57 | 32 | 91 | 32.4 | 56.9 | 3.3 |
| c | 94.9 | 16.0 | 98.7 | 13.4 | 0.7 | 0.62 | 37 | 106 | 25.0 | 40.1 | 2.4 |
| d | 97.8 | 19.2 | 102.3 | 13.1 | 0.9 | 0.62 | 37 | 127 | 23.5 | 37.7 | 2.2 |
| e | 146.2 | 13.9 | 149.5 | 33.4 | 1.3 | 0.63 | 37 | 134 | 40.9 | 65.4 | 4.0 |
| | | | | | | | | | mean: | n/a[††] | |
| CT8-6 | | | | | | | | | | | |
| a | 88.6 | 46.5 | 99.5 | 14.1 | 0.7 | 0.63 | 38 | 99 | 25.9 | 41.4 | 2.5 |
| b | 18.6 | 11.1 | 21.3 | 1.8 | 0.9 | 0.61 | 37 | 122 | 15.5 | 25.2 | 1.5 |
| c | 151.0 | 62.8 | 165.8 | 27.2 | 0.8 | 0.62 | 37 | 93 | 30.1 | 48.5 | 2.9 |
| d[#] | 67.6 | 48.4 | 78.9 | 7.7 | 0.5 | 0.50 | 28 | 94 | 17.8 | 35.4 | 2.1 |
| e[#] | 121.0 | 45.2 | 131.6 | 20.2 | 0.6 | 0.61 | 36 | 80 | 28.2 | 46.1 | 2.8 |
| | | | | | | | | | mean: | n/a[††] | |
| Western Qinghai Nan Shan | | | | | | | | | | | |
| CT8-7 | | | | | | | | | | | |
| a[#] | 13.0 | 61.4 | 27.4 | 14.5 | 0.4 | 0.50 | 27 | 100 | 95.0 | 190.0 | 11.4 |
| b[#] | 6.7 | 21.6 | 11.8 | 6.1 | 0.4 | 0.51 | 30 | 94 | 91.9 | 178.7 | 10.7 |
| c[#] | 19.1 | 39.6 | 28.4 | 9.3 | 0.5 | 0.52 | 30 | 76 | 59.4 | 114.0 | 6.9 |
| d[#] | 39.9 | 117.7 | 67.6 | 69.8 | 0.3 | 0.50 | 23 | 84 | 186.0 | 372.0 | 22.4 |
| | | | | | | | | | mean: | n/a** | |
| CT8-19 | | | | | | | | | | | |
| a | 13.1 | 46.3 | 24.0 | 21.1 | 1.6 | 0.62 | 39 | 169 | 158.6 | 255.5 | 15.3 |
| b[#] | 20.7 | 64.0 | 35.8 | 31.7 | 0.9 | 0.51 | 30 | 124 | 159.5 | 308.3 | 18.6 |
| c[#] | 5.2 | 22.4 | 10.4 | 6.0 | 0.4 | 0.54 | 32 | 78 | 103.5 | 192.5 | 11.5 |
| d[#] | 10.2 | 39.1 | 19.4 | 10.6 | 0.5 | 0.54 | 32 | 96 | 98.7 | 182.9 | 10.9 |
| e | 6.8 | 24.4 | 12.5 | 5.5 | 0.5 | 0.60 | 37 | 103 | 79.4 | 132.6 | 8.0 |
| | | | | | | | | | mean: | **194.1** | **122.90** |

*Ft correction from Ketcham et al. (2011).
[†]Assumed 6%, two standard deviation uncertainty for single-grain ages (Durango apatite reproducibility).
[§]Uncertainties on mean ages are 2 standard error (SE), from standard deviation among sample replicates.
[#]Single-grain ages rejected because grain radius <36 µm.
**No mean ages reported for samples with 0–1 single-grain ages for grains with radius ≥36 µm.
[††]No mean age reported because of correlation between eU and cooling ages.

of 6% for each single grain (based on the standard deviation of Durango apatite cooling ages; Farley, 2002). The remaining samples have an insufficient number of replicate ages from grains with $r > 36$ µm to report a mean cooling age.

For a subset of samples from the central part of the Qinghai Nan Shan and for samples from the Gonghe Nan Shan, apatite fission-track (AFT) analysis was performed, following methods outlined in Donelick et al. (2005). Spontaneous fission-track densities as well as the kinetic parameter $D_{par}$ were measured using an optical microscope ($n = \sim25$ for Qinghai Nan Shan samples and $n = \sim38$ for Gonghe Nan Shan samples), and $^{238}$U concentrations were measured using laser-ablation–inductively coupled plasma–mass spectrometry (Burtner et al., 1994; Ketcham et al.; Hasebe et al., 2004; Donelick et al., 2005). Confined track lengths, the angle between tracks and the crystallographic $c$ axis, and the kinetic parameter $D_{par}$ were also measured ($n = \sim125$ tracks for Qinghai Nan Shan samples and $n = \sim200$ tracks for Gonghe Nan Shan samples; Donelick et al., 2005). To visually assess dispersion of single-grain ages, we present radial plots for all samples, and all AFT data and summary information are presented in the Supplemental File (see footnote 1; Fig. 9; Galbraith, 2005; Vermeesch, 2009).

For most AFT samples, the ages are highly dispersed and not consistent with a singular age (Fig. 9; see also Supplemental File [see footnote 1]). Such high dispersion of single-grain fission-track ages is not surprising for sedimentary rocks, which may consist of apatites with multiple provenance thermal histories. However, it is noteworthy that plutonic rock samples CT8–4 and CT8–6 also have distributions that are not consistent with a common age (Fig. 9), despite
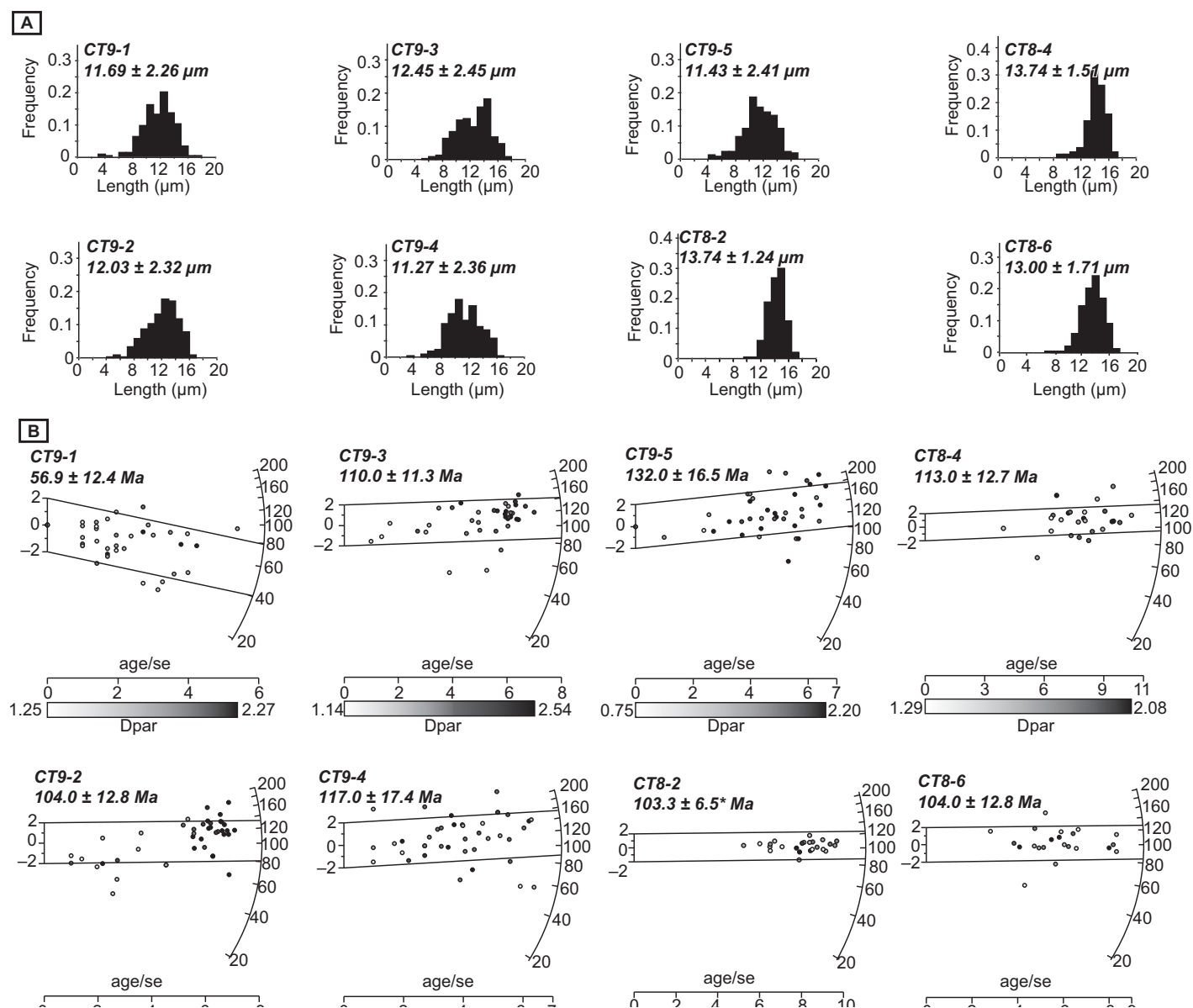
**Figure 9. (A) Track length histograms for apatite fission-track samples from the Qinghai Nan Shan and the Gonghe Nan Shan. Mean track lengths and one standard deviation are shown. (B) Radial plots of single-grain apatite fission-track ages from samples from the Qinghai Nan Shan and the Gonghe Nan Shan. All reported ages are central ages, except for sample CT8–2. Asterisk indicates single-grain age data from CT8–2 that appear to reflect a common value, so the pooled age is reported for this sample.**

the fact that grains from these two samples share an identical thermal history. For samples with age distributions that are not consistent with a common value (including CT8–4 and CT8–6), we report central AFT ages, and for the one sample with ages that appear to be consistent with a common value (CT8–2), we report a pooled cooling age (Fig. 9; Table 1; e.g., Galbraith, 2005). Reported uncertainties on both AFT central and pooled ages are two standard errors (Donelick et al., 2005; Galbraith, 2005; Vermeesch, 2009).

**Qinghai Nan Shan Cooling Histories**

In general, AFT cooling ages from the central Qinghai Nan Shan date to the Early Cretaceous (103–113 Ma; Fig. 9; Table 1). AHe cooling ages along the same transect range from approximately the middle of the Cretaceous to the Paleogene (46–110 Ma for mean ages, as well as single-grain ages as young as 25 Ma from lowest samples along transect, for which no mean ages are reported; Fig. 8; Tables 1 and

2). Single-grain ages from the western Qinghai Nan Shan are widely scattered and generally date to the Mesozoic. Because all single-grain ages are Paleogene or older, the age-elevation arrays of AHe and AFT data from the Qinghai Nan Shan indicate that exhumation of the range has been insufficient to exhume rocks that resided at temperatures higher than ~65 ± 5 °C (based on He-diffusion kinetics for the range of apatite compositions and cooling rates of ~1–10 °C/m.y.; Flowers et al., 2009), and far

less than necessary to exhume samples that were above the AFT closure temperature (~105 ± 10 °C, based on annealing kinetics for most common apatite compositions and cooling rates of ~1–10 °C/m.y.; Carlson et al., 1999; Ketcham et al., 1999; Reiners and Brandon, 2006).

We constructed an inverse time-temperature model of cooling pathways for sample CT8–6, using HeFTy v. 1.8.2.66 software (Ketcham, 2005). CT8–6 is the lowest, structurally deepest sample from the central Qinghai Nan Shan vertical transect (Fig. 10), which exhibits strong eU-age correlation. The model initiates at 250–200 Ma (approximately the Triassic, which is the likely emplacement age of plutons in the Qinghai Nan Shan based on regional map patterns), at a nominal temperature of 220–200 °C, e.g., sufficiently hotter than the closure temperature for the AFT and AHe systems. This model assumes simple, monotonic cooling, but we recognize that more complicated time-temperature histories involving burial and reheating could also be compatible with our data. We assume a modern surface temperature of 5 ± 5 °C. He diffusion kinetics for the apatite (U-Th)/He system are dependent on the degree of crystal radiation damage (determined from measured concentrations of U and Th; Flowers et al., 2009). Alpha particle stopping distances, and therefore alpha particle ejection age corrections, are from Ketcham et al. (2011). We specify four randomly generated subsegments in the time-temperature paths between our imposed constraints and require that time-temperature histories of these subsegments involve monotonic cooling. In the model, randomly generated Cenozoic cooling histories are generated and evaluated based on comparison to each of the three single-grain AHe cooling ages for CT8–6. Statistical evaluations of model-generated cooling histories are based on AHe data only. For the inverse model iterations, acceptable and good thermal histories are defined by 5% and 50% probabilities, respectively, where ages randomly drawn from the age distribution defined by empirical data are less similar to the empirical age distribution than the synthetic, model-defined data (see Ketcham, 2005). The inverse model was iterated 100,000 times, producing several hundred acceptable and good time-temperature paths (Fig. 11).

The model shows that for CT8–6, a relatively narrow range of time-temperature histories is permissible from ca. 55 to 25 Ma (Fig. 10). Permissible histories involve cooling through this time interval of perhaps ~30 °C, and no more than 40 °C. The model permits accelerated cooling after ca. 25 Ma; however, the timing is poorly constrained, and no acceleration in cooling is required. Prior to ca. 55 Ma, a wide range

of time-temperature cooling histories is permissible, including possible episodes of cooling and heating related to exhumation and reburial, and so we draw no conclusions about the history during this time.

**Gonghe Nan Shan Cooling Histories**

AFT ages from the central Gonghe Nan Shan generally date to the Early Cretaceous (Fig. 8), but the lowest sample along the transect has a younger age, of 57 ± 12 Ma, despite its proximity in depth and distance to other samples. Following the rationale described in the previous section, Neogene exhumation of the Gonghe Nan Shan must have been insufficient to exhume rocks that were at ~105 ± 10 °C (Reiners and Brandon, 2006).

Prior to attempting to construct an inverse for the lowest sample, CT9–1 (following the inverse modeling strategy employed for the Qinghai Nan Shan), we sought to understand the heterogeneity in AFT ages. We first filtered all single grains with ≤5 spontaneous fission tracks, because for these grains, the two standard error uncertainties on the cooling age exceeded the cooling age. The remaining 15 grains have $D_{par}$ values that range from ~1.4 to 2.3 μm, and, from these grains, we interpreted the presence of two distinct kinetic populations. For the nine grains with relatively low $D_{par}$ of 1.4–1.7 μm, the cooling ages are relatively young, ranging from 15 to 59 Ma, and mean track length is 13.5 ± 1.3 μm (*c*-axis projected, 1 standard deviation). The six grains ranging from $D_{par}$ of 1.7 to 2.3 μm pass a chi-squared test, indicating that the age distribution is consistent with a common value. The pooled age of these six grains is 80.8 ± 20.1 Ma (2 standard errors), and the mean track length of 58 tracks with overlapping $D_{par}$ is 13.6 ± 1.1 μm (*c*-axis projected, 1 standard deviation). The cooling age–$D_{par}$ correlation, in

which high $D_{par}$ grains have relatively old cooling ages (e.g., Burtner et al., 1994), is consistent with the interpretation that AFT ages for CT9–1 were annealed and reset following the Triassic and, additionally, implies that these grains likely spent a protracted amount of time in the AFT partial annealing window during cooling subsequent to maximum burial.

For the inverse modeling of CT9–1, we initiated models at near-surface temperatures at 250–200 Ma, in order to approximately overlap with the depositional age of the Songpan-Ganzi strata. The only additional constraint we imposed is that maximum burial temperatures were above the AFT closure temperature and were achieved prior to the Cretaceous, based on the ages of the various AFT samples from the Gonghe Nan Shan vertical transect. In the inverse models, fission-track lengths were normalized based on the angle from the crystallographic *c* axis (Ketcham et al., 2007a), and fission-track annealing kinetics are from Ketcham et al. (2007b). In light of the apparent presence of multiple kinetic populations, we present three different inverse models for CT9–1, one in which the model is statistically constrained by both AFT kinetic populations (Fig. 10B) and two more in which the model is statistically constrained by either the low $D_{par}$ or the high $D_{par}$ kinetic populations (Figs. 10C and 10D, respectively). Good and acceptable model iterations were determined in the same way as described for sample CT8–6, except that the Gonghe Nan Shan models were optimized using both AFT pooled age and length measurements (see Ketcham, 2005). The inverse models were iterated 100,000 times, producing several hundred acceptable and good time-temperature paths.

In general, all of the CT9–1 inverse model results for the Gonghe Nan Shan are strikingly similar to the Qinghai Nan Shan results (Fig. 10). From 80 to 15 Ma, a modest amount

**Figure 10 (*on following page*). Inverse time-temperature models for Qinghai Nan Shan (U-Th)/He (AHe) sample, CT8–6, and Gonghe Nan Shan apatite fission-track (AFT) sample CT9–1. Models were generated in HeFTy (Ketcham, 2005). Green paths show acceptable thermal histories (goodness-of-fit statistic of 0.05 calculated from empirical and synthetic cooling ages and track lengths), and purple paths show good thermal histories (goodness-of-fit statistic of 0.5). (A) Inverse model for Qinghai Nan Shan sample CT8–6. (B–D) Inverse model for Gonghe Nan Shan sample CT9–1. In B, inverse model is statistically constrained by two kinetic populations with low and high values of $D_{par}$. In C and D, inverse models are statistically constrained with only the low and high $D_{par}$ kinetic populations, respectively. Although the low (C) and high (D) $D_{par}$ models both yield numerous "good" time-temperature paths, they overlap for only a narrow temperature range in the time period from ca. 80–20 Ma, such that model B has a relatively small number of acceptable time-temperature paths. Graphs to the right of time-temperature plots in B–D show single grain cooling ages and pooled cooling ages (with 1 standard error), and track length measurements and mean track lengths (with 1 standard deviation) for kinetic populations, plotted against $D_{par}$.**
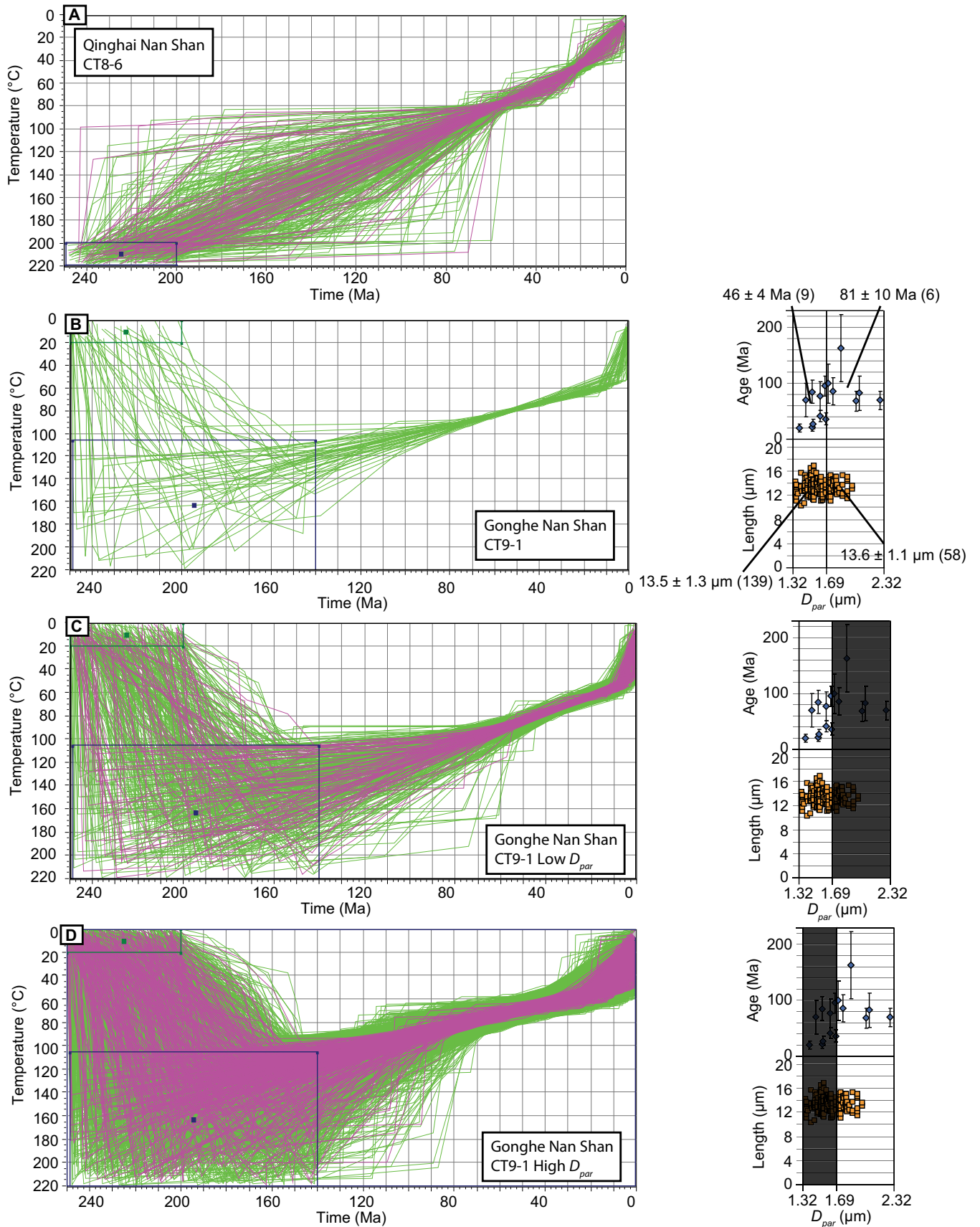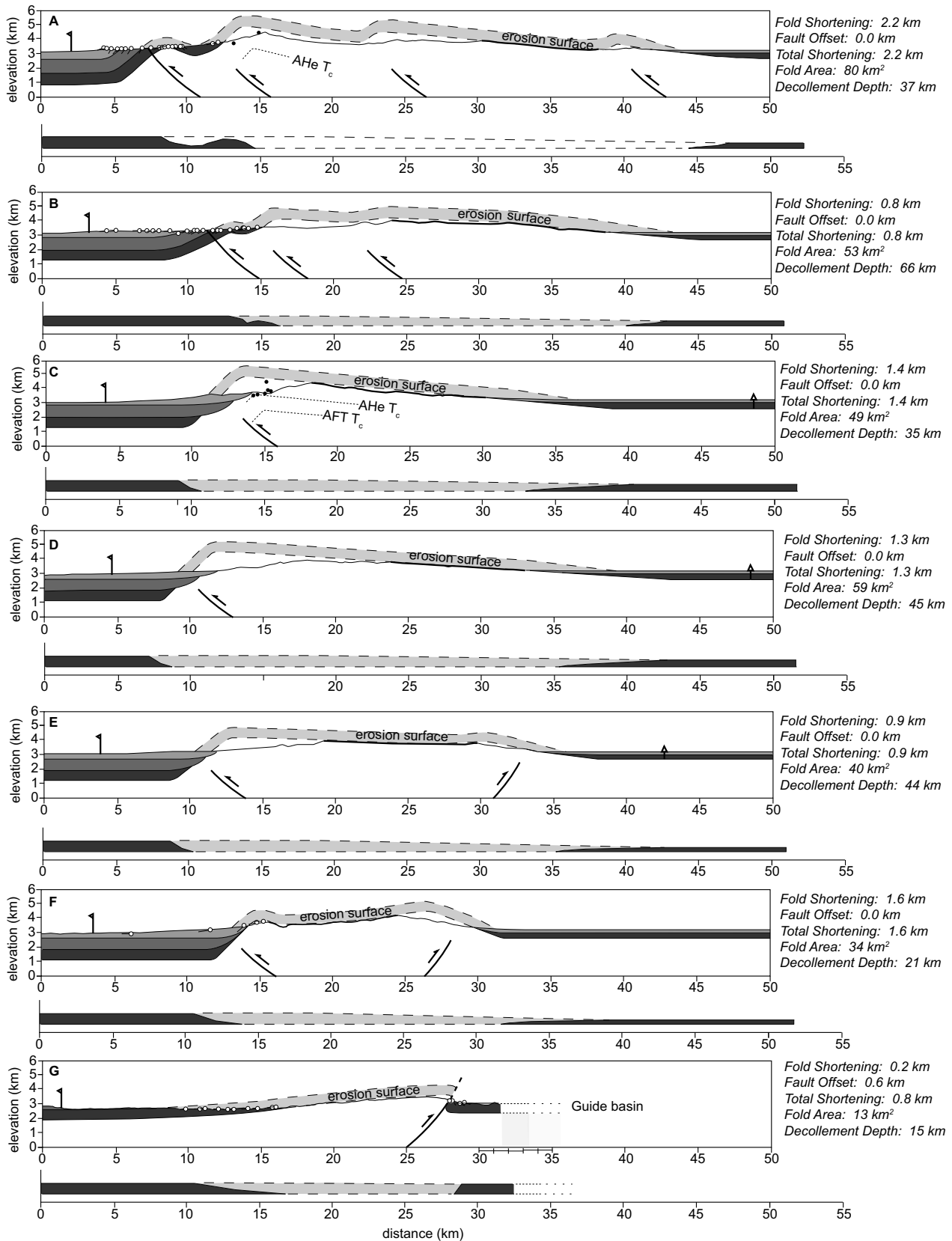
**Figure 10.**

**Figure 11. Serial deformed-state and restored cross sections through the Qinghai Nan Shan, for the Neogene-Quaternary. Only pre-growth strata are shown in restored sections. Locations of cross sections are shown in Figure 4. The locations of thermochronology sites are shown by closed black circles. AHe—apatite (U-Th)/He; $T_c$—closure temperature; AFT—apatite fission track.**

of cooling is permissible, most likely ~20 °C and not more than 40 °C. The model suggests a modest acceleration in cooling at some time after ca. 15 Ma, and a range of time-temperature histories is possible prior to the Cenozoic (Fig. 10B). Although cooling histories implied by inversion of the low $D_{par}$ and high $D_{par}$ data are similar, a relatively narrow range of time-temperature paths overlaps with acceptable cooling histories for the two populations, such that the model that is constrained by both populations yields fewer acceptable cooling histories and no good fits compared to the models run against restricted $D_{par}$ values (Fig. 10B). The slightly higher temperatures that optimize the relatively low $D_{par}$ model (in comparison to the high $D_{par}$ model) are consistent with the fact that low $D_{par}$ grains are less annealing resistant, experience more annealing, and are therefore optimized by cooling histories involving relatively high temperatures.

**Thermochronologic Bounds on Structural Relief**

The AFT and (U-Th)/He ages and inverse models facilitate an evaluation of structural relief in the hanging-wall ranges of the Qinghai Nan Shan and Gonghe Nan Shan fault systems. Reconstruction of paleodepth of a sample just prior to faulting gives a minimum vertical displacement across the fault or total displacement if correlative markers are known in the footwall block (Clark and Bilham, 2008; Zheng et al., 2010), and this analysis is useful for evaluating the degree to which deformed-state cross sections through the two ranges (presented next) are admissible (sensu Woodward et al., 1989). We assume nominal AHe and AFT closure temperatures (described earlier herein), and a typical continental geothermal gradient of 20–30 °C/km for all of the burial depth reconstructions. Although simple, a linear geothermal gradient is likely to be a reasonable approximation for the relatively shallow crustal levels and limited exhumation considered here.

For the central Qinghai Nan Shan, the time-temperature modeling indicates that at the end of the Paleogene, sample CT8–6 experienced temperatures of ~50 ± 10 °C (Fig. 10). This is generally consistent with the cooling ages for the lower samples from the central Qinghai Nan Shan transect (all but CT8–4, ~0.5–1.0 km below the erosion surface; Fig. 8). At typical geothermal gradients, this suggests that CT8–6 was buried by 1–3 km of material, which is in the range of the depth of CT8–6 below the Qinghai Nan Shan erosion surface and, presumably, Neogene structural relief. Notably, these paleodepth calculations permit up to ~2 km of

sedimentary cover atop the Qinghai Nan Shan erosion surface during the Paleogene to achieve burial depths of 3 km (Fig. 10), although no such sedimentary cover appears to be required by the data.

In the Gonghe Nan Shan, thermal models suggest that sample CT9–1 resided at 65 ± 10 °C near the end of the Paleogene (Fig. 10). Assuming typical geothermal gradients, this suggests that the sample was at a depth of ~2–4 km and was unlikely to have been much deeper, given the Cretaceous AFT central ages of higher samples. Thus, these data bracket the Neogene structural relief of the Gonghe Nan Shan and imply that the structural depth of the samples would have been sufficient to explain their thermal history. That is, no Paleogene sedimentary cover would have been required to achieve the estimated paleodepth.

**SHORTENING RATES FROM BALANCED CROSS SECTIONS**

In order to reconstruct Cenozoic deformation across the Qinghai and Gonghe Nan Shan, we developed a series of balanced cross sections and measured the line-length shortening recorded along each (Figs. 4, 6, 11, and 12). Several assumptions and simplifications were made in order to construct these structural models; we discuss these in the context of each range next. However, in general, our shortening estimates are minimums, involving straight fold limbs, kink-band fold geometry, and minimized offsets of piercing points. For both fault systems, we assumed that folding was accommodated by shear parallel to bedding, such that stratigraphic horizons are lines of no finite longitudinal extension (Dubey and Cobbold, 1977).

For the Qinghai Nan Shan sections, we used structural measurements along the southern range front and geomorphic observations from the northern flank of the range to constrain deformed-state fold geometry. We ensured that inferred structural depths are in accord with the constraints provided by the AFT and AHe data from the range. We assumed that the fold limbs projected and intersected approximately above the topographic divide of the range, and that these limbs were not offset by faulting. In the central part of the range, the structural culmination must be shifted to the south of the modern topographic divide by at least 1–3 km, given the observed pattern of AHe cooling ages along section 11C (Fig. 11C), and the position of the bedrock–basin fill contact (see Fig. 11E, for example). Where the erosion surface on the northern flank of the range is buried by Qinghai Lake basin fill, we projected the dip of the north limb of the Qinghai Nan Shan beneath the basin

to a depth of ~500 m, which is the lower bound for the thickness of sediment beneath southern Qinghai Lake (An et al., 2006), making the basement slightly higher on the north side of the range compared to the south side. At that point, we assumed that the north limb passes through a kink band and becomes horizontal. Projecting to a greater depth would slightly increase the shortening recorded by the cross section. Perhaps the most speculative assumption is that in the western part of the range (in the vicinity of Chaka) and in the eastern part of the range, we assumed that the prominent topographic saddle (see Figs. 4 and 5) marks the presence of a second fault system, such that the range is a composite of two large-scale imbricate faults. We made this assumption because in other parts of the interior of the range, the topography closely mimics the structural architecture (Fig. 5).

For the Gonghe Nan Shan sections (Figs. 6 and 12), we assumed that the southern margin of the range is marked by a thrust fault and that the topographic saddle in the eastern half of the range defines a structural saddle between two imbricated thrust sheets. We constrained the forelimb geometry using the attitude of tilted beds in the adjacent foreland and the back limb geometry by projecting structural measurements southward toward the fault plane. This assumption appears to be consistent with thermal data from the southern flank of the range because the preferred deformed-state geometry indicates that the AFT samples correspond to ~3.1–3.5 km of bedrock structural depth (Fig. 12C). We constructed the western cross sections (Figs. 12A and 12B) so that they exhibit a similar back-limb architecture as section 12C (Fig. 12C). We minimized the depth of footwall cutoffs of Neogene strata that predate range growth. Finally, we assumed that the north limb of the fold extends northward until it is ~1500 m below the basin fill top, based on measured stratigraphic thickness in southern Gonghe (Craddock et al., 2011a).

Restoration of the deformed-state cross sections suggests that the present-day geometries reflect relatively limited shortening across the Qinghai Nan Shan, on the order of ~1.5 ± 0.7 km (Fig. 11). Notably, the higher shortening estimates come from the far eastern and far western parts of the range (1.6–2.2 km), where the presence of multiple imbricate structures appears to require greater total shortening. Along the central part of the range, where the fault system appears to consist of a single structure, shortening estimates range between 0.9 and 1.4 km. Given that the width of the range is ~30–40 km, our budgets imply that Cenozoic shortening is less than 10%, and perhaps as low as ~3%. Based on the geologic and stratigraphic
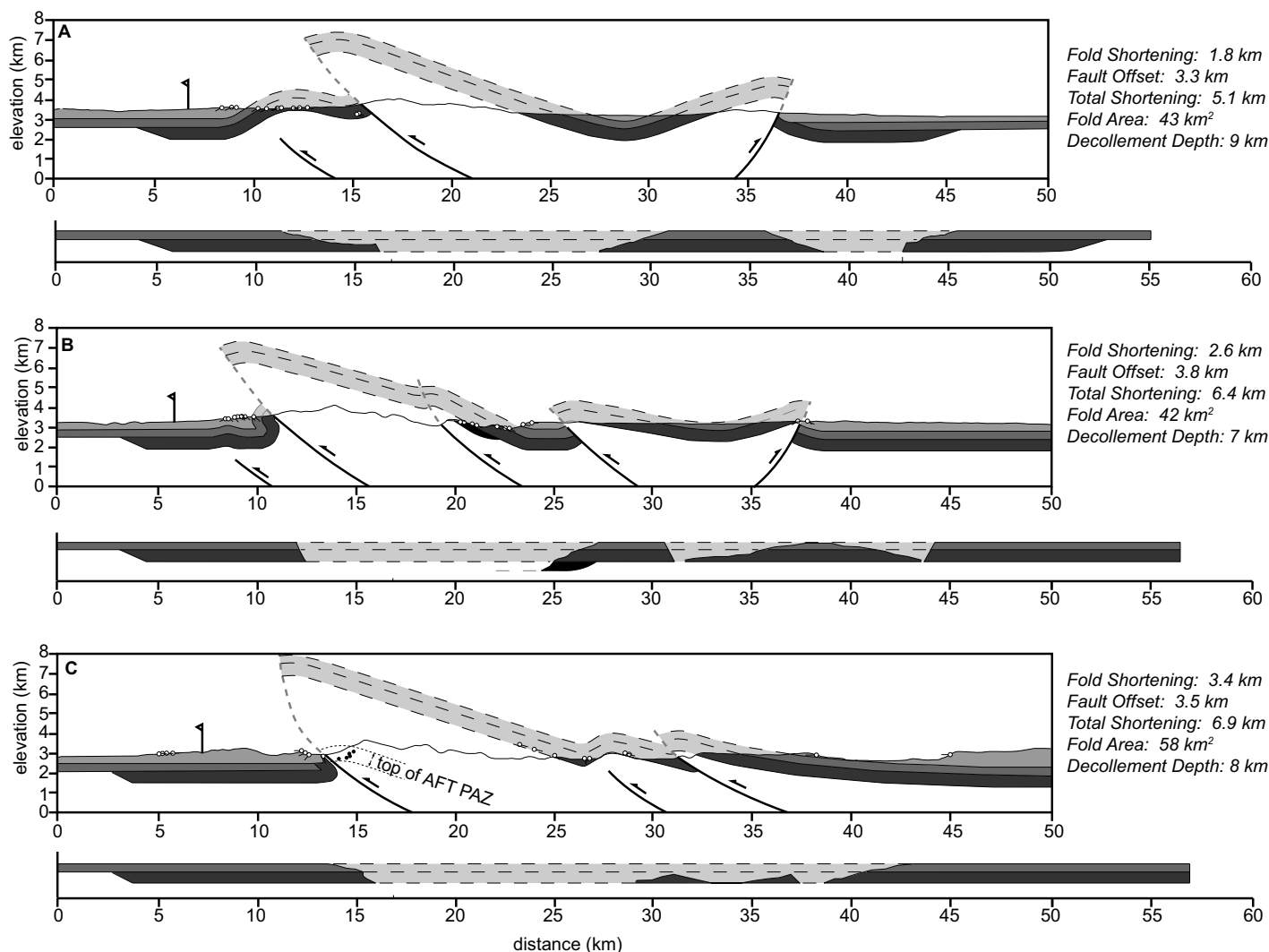
**Figure 12. Serial deformed-state and restored cross sections through the Gonghe Nan Shan, for the Neogene-Quaternary. Only pregrowth strata are shown in restored sections. Restored sections show only pregrowth strata. The locations of the cross sections are shown in Figure 6. The locations of thermochronology sites are shown by closed black circles. AFT—apatite fission track; PAZ—partial annealing zone.**

data summarized here, we consider an initiation age for range growth along the Qinghai Nan Shan of 8 ± 2 Ma (Fang et al., 2005; Lease et al., 2007; Yuan et al., 2011; Zhang et al., 2012; Lu et al., 2012). This implies average shortening rates of ~0.2 +0.2/–0.1 km/m.y. since the late Miocene.

Line-length measurements of shortening across the Gonghe Nan Shan are slightly greater, ~6.0 ± 0.9 km (Fig. 12). Given that the width of the range is 20–30 km, this implies correspondingly greater shortening across the range (15%–26%). Foreland basin stratigraphic archives adjacent to our restored cross sections bracket the initiation of faulting to ca. 8.5 ± 1.5 Ma (Craddock et al., 2011a), and this result implies that average shortening rates range around ~0.7 +0.3/–0.2 km/m.y. since the late Miocene.

## LATE QUATERNARY SLIP RATES ALONG THE QINGHAI NAN SHAN

### Quaternary Geologic Mapping of Qinghai Nan Shan Range Front

A sequence of well-exposed alluvial-fan deposits is preserved along the southern flank of the Qinghai Nan Shan (Fig. 13). In the proximal footwall of the range, multiple generations of these alluvial surfaces are associated with well-defined fault scarps that strike subparallel to the range front (Fig. 13). Because displaced depositional surfaces can serve as structural markers for reconstructing fault slip rates, we present detailed observations of several generations of alluvial surfaces at a site that is ~5 km from the western structural transect along the

western Qinghai Nan Shan (Fig. 4). Several alluvial surfaces can be identified in the field and from satellite imagery (Fig. 13). These generations include (1) the abandoned depositional surface in the uplifted hanging wall of the fault and intervening active channels in the footwall of the fault, (2) several generations of terraces in the uplifted alluvium, and (3) low terraces perched above active channels in the footwall of the fault.

We focus on the Qf2 surface because it is present in both the footwall and hanging-wall blocks (Fig. 13) and therefore provides a useful structural marker. We conducted topographic surveys perpendicular to the fault trace that deforms Qf2 using a total station (Fig. 13). The surface itself is relatively well preserved in the uplifted block and becomes progressively
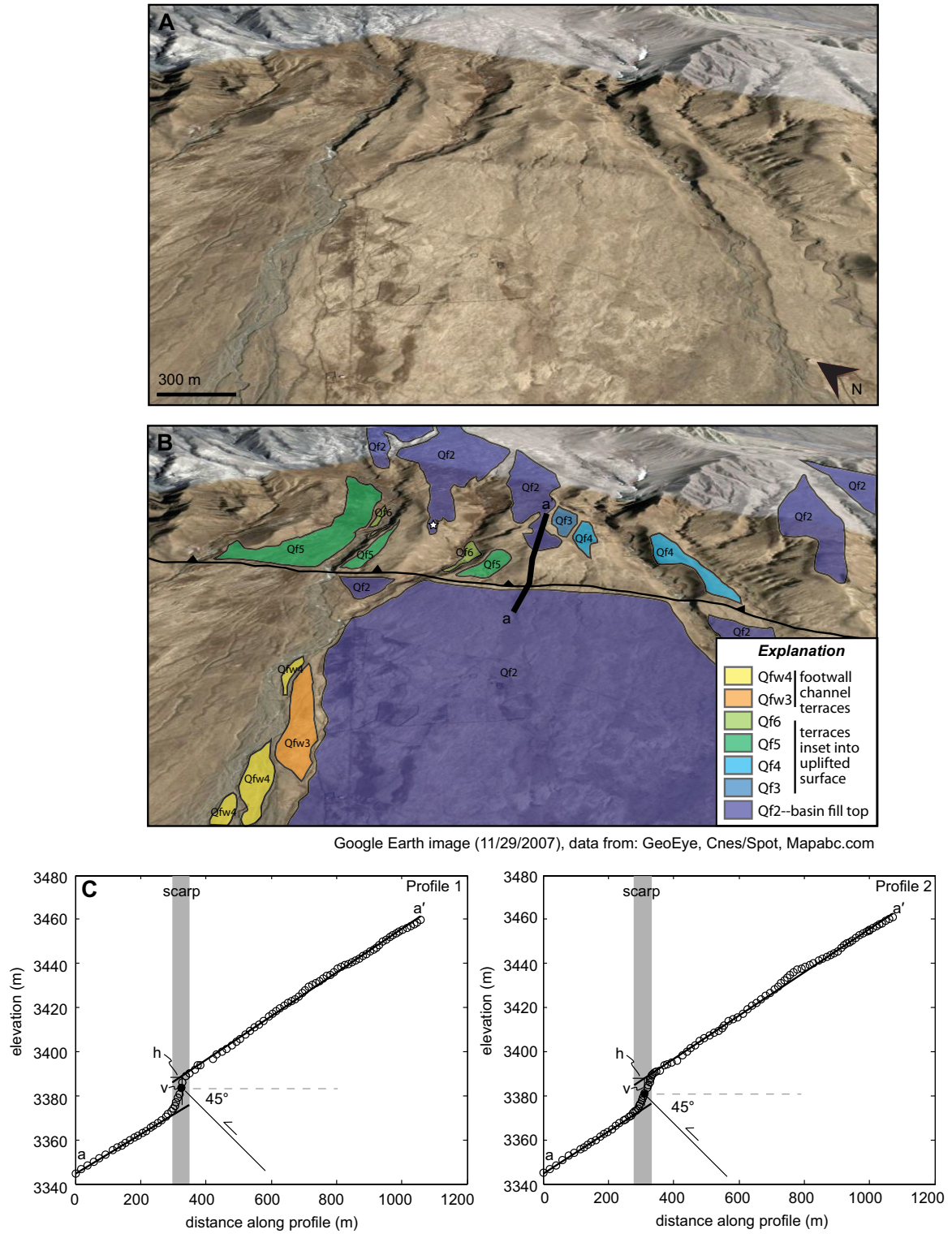
Figure 13. (A) Deformed alluvial-fan surface near Chaka. Image location is shown on Figure 4. Image is from Google Earth, and map data are copyrighted by GeoEye, Cnes/Spot, and Mapabc.com. Image date is 29 November 2007. (B) Interpretation of correlative fan surfaces. Star shows location of soil pit (shown in Fig. 14). Line shows location of topographic surveys. (C) High-resolution topographic profiles (open circles) measured across deformed alluvial-fan surface. Profile 1 is ~20 m to the NW of profile 2. We assume a fault dip of 45.0° (shown schematically on figure) with a standard deviation of 7.5°. Closed circles in the middle of scarps represent scarp midpoint (in the along-profile dimension). Lines through upper and lower alluvial surface segments are linear regressions. Due to the length of the profiles, lines with slope of ±2 standard deviations and passing through the midpoint of the segments plot on top of best-fit regression lines. h—horizontal; v—vertical.

dissected near the fault scarp and along incised gullies (Fig. 13). Field observations indicate that the Qf2 surface in the hanging wall of the fault is topographically smooth, absent any original depositional morphology. An ~3-m-deep soil pit reveals a relatively simple stratigraphy (Fig. 14). The upper 20 cm section of the pit consists primarily of silt (75%), with pebble-sized clasts in the silt-rich matrix. Between 20 and 25–35 cm, the proportion of silt decreases and remains relatively constant with depth (~35%–40%). We infer that at least some of the high concentration of silt reflects eolian input/inflation of the abandoned surface. At 25–35 cm depth, a 1-cm-thick, unbroken, wavy band of pedogenic carbonate extends across the pit wall. Clasts beneath this horizon exhibit carbonate coatings to a depth of ~50 cm. Below this band, the lower 260–270 cm section of the pit contains clast-supported, conglomeratic alluvial deposits, with 35%–50% matrix material. Clasts are granules

and pebbles, and *b* axes are as large as a few tens of centimeters. The presence of pedogenic carbonate suggests the development of a soil atop the preserved depositional surface, over at least tens of thousands of years (Ludwig and Paces, 2002; Candy et al., 2004). With the exception of the pedogenic carbonate, which is covered by 25–35 cm of loess in the upper part of the profile, we see no evidence for significant burial/excavation of soil horizons.

## Abandonment Age of Qf2

We sampled along a depth profile to determine the in situ accumulation of $^{10}$Be in quartz samples below the Qf2 surface (Figs. 3, 13, and 14); this site was chosen near the center of the relict surface to minimize the effects of erosion and surface degradation near incised channels. We collected >250 clasts, with *b*-axis diameters of 0.5–1.5 cm, from 5-cm-thick layers along

seven different stratigraphic horizons. The highest sample was collected at 40 cm depth, below the silt-rich horizon, because this appears to be the shallowest horizon undisturbed by loess inflation. Samples were collected to a depth of ~3 m, because at this depth spallogenic cosmogenic isotope production occurs at negligible rates (Fig. 13; e.g., Anderson et al., 1996; Hancock et al., 1999), and cosmogenic inventories are inferred to largely reflect inherited $^{10}$Be inventory prior to sediment deposition. We measured $^{10}$Be inventories for these samples following standard protocols at PRIME Laboratory at Purdue University. Laboratory techniques are described in detail in the Appendix.

Measured $^{10}$Be inventories range from 49.9 × $10^5$ atoms of $^{10}$Be per gram of quartz at the shallowest sample in the depth profile (40 cm), to 2.8 × $10^5$ atoms of $^{10}$Be per gram of quartz at the base of the profile (300 cm; Fig. 14; Table 3). Visual inspection of the depth profile suggests
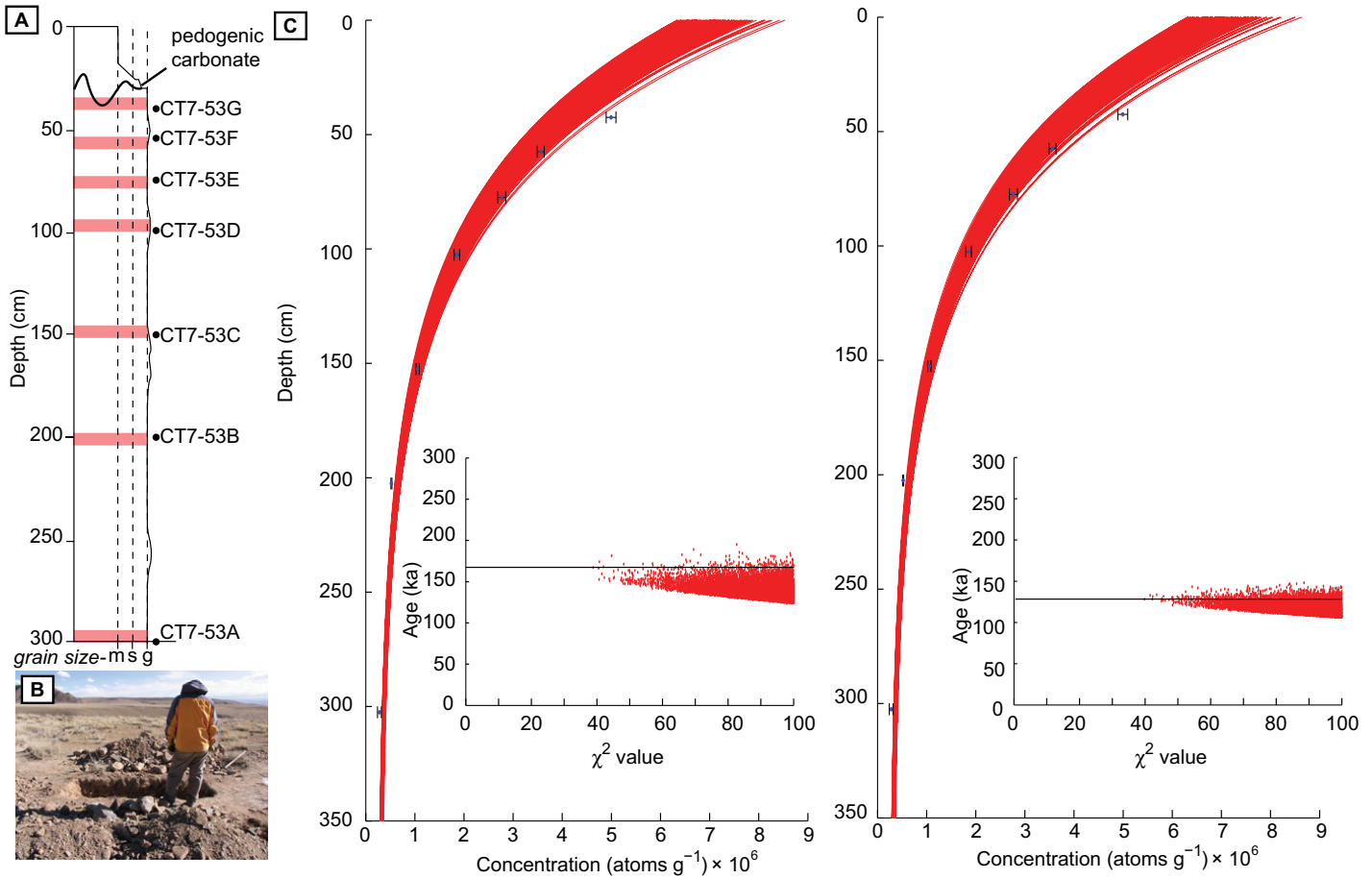


Figure 14. (A) Soil pit stratigraphy and cosmogenic sample sites. m—mud; s—sand; g—gravel. (B) Image of soil pit, showing abandoned surface in hanging wall of the fault in the background. (C) Surface abandonment age calculations, assuming (from left to right) a stable surface and inflation by 0.2 cm/k.y. Graphs show measured cosmogenic inventories from depth profile plotted above synthetic depth profiles, which reflect probabilistic ranges of soil density and abandonment age. For all scenarios, we iterated 10,000 model runs, and synthetic data satisfied a chi-squared threshold value of 100.

TABLE 3. $^{10}$Be DEPTH PROFILE

| Sample | PRIME Lab ID | Depth (cm) | Sample wt. (g) | Carrier wt. (mg) | Target wt. (mg) | $^{10}$Be/total Be[†] | Error | $^{10}$Be (atoms/g*) | Error (atoms/g*) |
|---|---|---|---|---|---|---|---|---|---|
| CT7-53A | 200803136 | 300 | 12.9140 | 0.30668 | 0.68091 | 178.70 | 24.17 | 278,858 | 38,394 |
| CT7-53B | 200803137 | 200 | 44.0020 | 0.37959 | 0.84277 | 910.40 | 20.44 | 523,142 | 11,798 |
| CT7-53C | 200803138 | 150 | 22.1370 | 0.36604 | 0.81270 | 958.70 | 26.25 | 1,056,123 | 29,029 |
| CT7-53D | 200803139 | 100 | 13.9610 | 0.30729 | 0.68226 | 1264.00 | 32.46 | 1,854,948 | 47,772 |
| Blank (A–D) | 200803135 | | | 0.37928 | 0.84210 | 2.89 | 0.96 | | |
| CT7-53E | 200803140 | 75 | 17.8590 | 0.31855 | 0.70727 | 2321.00 | 73.47 | 2,766,843 | 87,583 |
| CT7-53F | 200803141 | 55 | 23.8170 | 0.37061 | 0.82284 | 3426.00 | 110.10 | 3,562,837 | 114,498 |
| CT7-53G | 200803142 | 40 | 32.3250 | 0.37670 | 0.83635 | 6411.00 | 129.20 | 4,992,972 | 100,623 |
| Blank(E–G) | 200803143 | | | 0.37806 | 0.83940 | 0.00 | 0.26 | | |

*Note:* 36.7703°N, 99.2951°E, 3451 m.
*Units are atoms of $^{10}$Be per gram of quartz.
[†]Mantissa of $^{10}$Be/total Be = 1 × 10$^{-15}$.

an approximate exponential decay in cosmogenic $^{10}$Be concentration with depth (Fig. 14). At the lowest part of the profile, $^{10}$Be concentration is nearly invariant with depth, so we take the 2.8 × 10$^5$ atoms of $^{10}$Be per gram of quartz to represent the best estimate of an inherited component of cosmogenic $^{10}$Be.

In order to calculate the surface abandonment age, we used an approach that incorporates probabilistic constraints on key geologic variables to estimate the abandonment age of a depositional surface (Hidy et al., 2010). The approach incorporates uncertainties in isotope half-life, production rate, soil density, lowering/inflation rate, inherited isotope inventory, and neutron attenuation length. Moreover, the approach accounts for topographic shielding, surface attitude, and periodic cover by loess and/or snow. We utilized a $^{10}$Be half-life of 1.387 Ma (±5%) and a reference production rate of 4.76 atoms of $^{10}$Be per gram of quartz per year (Nishiizumi et al., 2007). We used the scaling scheme of Stone (2000) to calculate production rates at our local site. Based on visual inspection of the depth profile, initial inheritance was set at 280,000 ± 40,000 atoms of $^{10}$Be per gram of quartz. We assumed soil density of 1.8–2.2 g cm$^{-3}$ (e.g., Champagnac et al., 2010), and set a neutron attenuation length of 160 ± 5 cm (Gosse and Phillips, 2001). Due to the proximity of the sample site to an adjacent mountain range front, we measured the angle to the horizon, at 15° intervals, for a 360° spectrum. The topographic shielding factor at this site is ~0.999, such that it is negligible.

The critical uncertainty in determining the abandonment age of the Qf2 surface is accounting for the history of soil inflation by loess and/or postabandonment lowering of the depositional surface (Cerling and Craig, 1994). In order to explore the influence of various surface histories on the abandonment age, we present two end-member scenarios (Fig. 14). In the first, we assume that the depositional surface has been completely stable since abandonment. This is likely an unrealistic assumption, but this

scenario provides a useful frame of reference for evaluating the importance of inflation/erosion. This assumption yields a most probable abandonment age of 164 +6/–20 ka (2σ confidence limits). However, given the high percentage of silt-sized particles in the upper part of the soil profile (upper 30 cm), we consider it more likely that some inflation of the surface occurred during loess deposition; this process will tend to reduce calculated abandonment ages, as shallow material is advected to deeper levels of the soil profile. Thus, in the second scenario, we assume that the loess in the soil profile accumulated steadily, at a rate of ~0.2 cm/k.y. This rate is roughly equivalent to 30 cm of loess inflation in 150 k.y. In both the Gonghe and Tongde basins, optical dating of loess deposits that cap multiple generations of late Quaternary river terraces indicates that loess accumulation began ca. 130–150 ka (Harkins et al., 2007; Craddock et al., 2010; Perrineau et al., 2011), suggesting that our modeling scenario is a reasonable lower bound. In this end-member scenario, the most probable abandonment age is 129 +5/–7 ka.

Clearly, modification of the alluvial surface following abandonment strongly influences the exposure age calculation. We consider that scenario 1, in which the surface was stable, and scenario 2, in which loess accumulated steadily following abandonment, bracket the true abandonment age of the Qf2. As such, we suggest that 130–160 ka is a reasonable range of ages for the timing of surface abandonment.

### Late Quaternary Shortening Rates

We reconstructed fault slip by fitting linear regressions to the topographic survey data from the Qf2 surfaces and projecting these surfaces to their intersection with a planar fault (following the approach of Thompson et al., 2002; see Figs. 14 and 15). Linear regressions were performed for both the hanging-wall and footwall alluvial-fan surfaces, and survey data from the fault scarp were excluded from the regressions. Linear regression through survey data indicates

that the alluvial-fan surface has slopes of 5.3° ± 0.1° to 5.7° ± 0. 1° (at 1σ). We assumed that the fault plane intersects the midpoint of the fault scarp and estimated uncertainties using a Monte Carlo approach that considers uncertainties in both the alluvial surfaces and fault dip (following Thompson et al., 2002). We allowed both parameters to vary according to Gaussian probability distributions (Figs. 15A and 15B). Although fault dip is poorly constrained at this site, several observations from similar structures throughout the Qilian Shan suggest that 45.0° ± 7.5° (1σ) is a reasonable range (e.g., Peltzer et al., 1988; Zhang et al., 1991; Avouac and Tapponnier, 1993; Meyer et al., 1998).

We calculated vertical offsets of 13.2 ± 0.4 m for scarp profile 1 and 11.8 ± 0.4 m for scarp profile 2 (Fig. 15C). Reported uncertainties are 1σ. Geometrically, these values for fault throw imply 19.1 ± 2.4 m of total slip and 13.6 ± 3.5 m of horizontal slip along profile 1 and 17.1 ± 2.0 m of total slip and 12.2 ± 3.0 m of horizontal slip along profile 2 (Fig. 15C). By integrating these displacement calculations with the abandonment age calculation, we find minimum throw rates across the fault of ~0.09 ± 0.02 mm/yr and shortening rates of ~0.10 ± 0.04 mm/yr.

### DISCUSSION

#### Fault Geometry at Depth

Coupled with the low magnitude of shortening across the ranges, the broad, gently dipping back limbs of the Qinghai and Gonghe Nan Shan are compatible with a fault geometry that becomes curviplanar at depth (e.g., Suppe, 1983; Amos et al., 2007). Similar geometries have been inferred for contractional structures in the neighboring Guide and Xunhua regions (Lease et al., 2012b). Moreover, the broad, range-scale anticlines and the modest amounts of shortening across the ranges imply that faults likely sole into relatively deep ductile shear zones in the mid- to lower crust. Under the assumption of plane strain, we use the constraint that the cross-sectional area
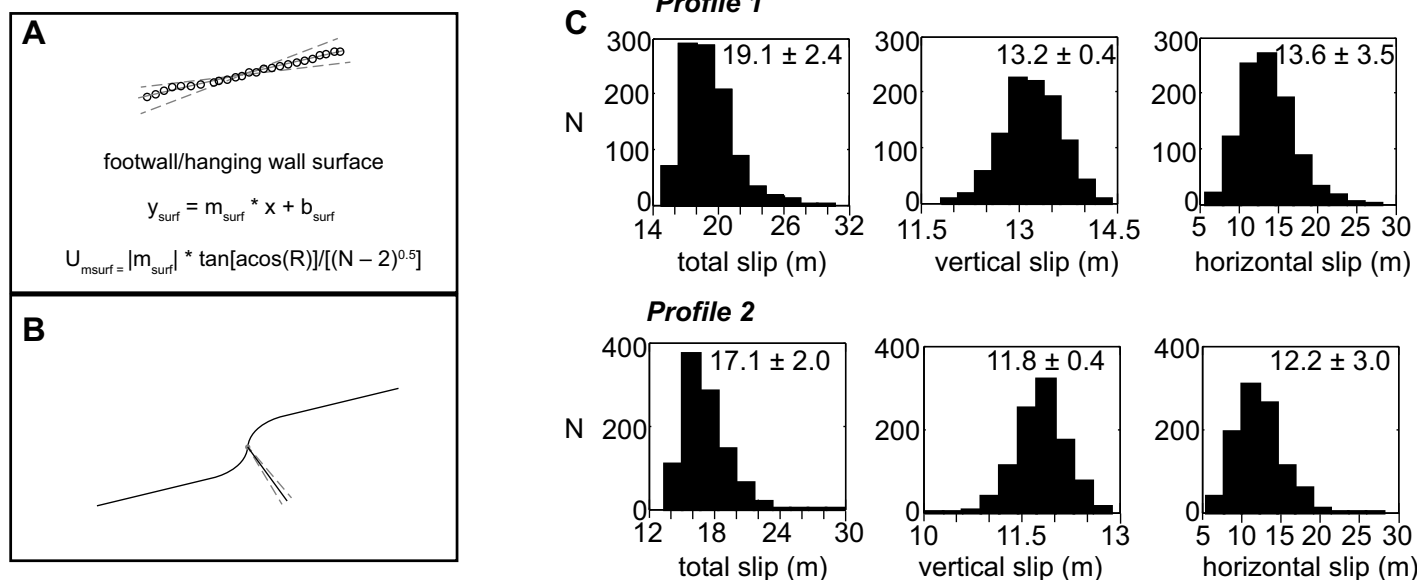
**Figure 15. Fault-slip reconstruction. (A) Method of linear regression for upper and lower alluvial-fan surfaces. (B) Fault dip estimation. We assume a fault dip of 45° with a standard deviation of 7.5°. (C) Total slip, vertical slip, and horizontal slip reconstructions for topographic profiles through Chaka fault scarp.**

of a fold above an undeformed datum should be balanced by the product of line-length shortening and effective detachment depth (e.g., Woodward et al., 1989) to estimate detachment depths for each of our cross sections (Figs. 11 and 12). This calculation implies that, across the width of the Qinghai Nan Shan, the range-bounding fault is likely to extend at least into the middle crust (at least ~30 km). It is plausible that the fault system could extend tens of kilometers deeper, suggesting a limit on the depth of putative crustal channels below the northeastern plateau margin (e.g., Clark and Royden, 2000), although the highest of our décollement depth estimates seem untenable in light of likely crustal thicknesses of ~54 ± 6 km in the region (Vergne et al., 2002; Galvé et al., 2002; Yang et al., 2012).

The depth extent of fault systems in the Qinghai Nan Shan is also consistent with the mechanical properties of the middle-upper crust inferred from geophysical data. Analyses of crustal conductance, Vp/Vs ratios, Bouguer gravity anomalies, and shear wave velocities all suggest that localized regions of relatively low-viscosity crust appear to be confined to the region proximal to the Kunlun fault and regions to the south (Wei et al., 2001; Vergne et al., 2002; Jordan and Watts, 2005; Yang et al., 2012). The crust beneath the northeastern Tibetan Plateau appears to be comparatively either colder, more rigid, or both (Klemperer, 2006).

In contrast, the fault system beneath the Gonghe Nan Shan appears to sole into a relatively shallow décollement, at depths between

7 and 9 km. The relatively shallow décollement of the Gonghe Nan Shan probably reflects the bedrock geology underlying the Gonghe Basin complex. Basement rocks across most of the Gonghe region are covered by a thick succession of Triassic flysch that extends to the south and covers the entire Songpan-Ganzi terrane (Fig. 2; Yin and Harrison, 2000). Although the precise thickness of the Triassic strata in the southern Gonghe region is not well known, regional map patterns suggest that the thickness is between 5 and 15 km in the interior parts of northeastern Tibet (GBGMR, 1989). Active source seismic profiling suggests that the Songpan-Ganzi flysch may be as thin as ~2 km beneath Tongde sub-basin, and possibly as thick as ~10 km (Zhang et al., 2011). Much of the Songpan-Ganzi flysch is interpreted to have been deformed above a regionally extensive décollement in the Late Triassic (Burchfiel et al., 1989). Although it is not clear whether this décollement is present at depth beneath the Gonghe region, the correspondence between likely stratigraphic thickness of the Triassic strata and the calculated depth of the Gonghe Nan Shan fault system suggests that the mechanical discontinuity at the base of the Triassic may represent the primary detachment horizon for the Gonghe Nan Shan fault network (Fig. 16).

In light of the constraints that our structural reconstructions place on the crustal architecture of the Gonghe region, we propose a simple cross-sectional model for the Qaidam-Qilian terrane, wherein the Qinghai Nan Shan fault

system extends to deep crustal levels and the Gonghe Nan Shan fault system detaches along the sub-Triassic unconformity (Fig. 16). In addition to the various constraints on the structure of the upper crust (Fig. 2; GBGMR, 1989; QBGMR, 1991) and the deep architecture of major regional fault networks, we have incorporated approximate Moho depths from seismic-reflection and seismic-refraction experiments (Galvé et al., 2002; Vergne et al., 2002; Jiang et al., 2006; Liu et al., 2006; Zhang et al., 2011; Wang et al., 2011; Yang et al., 2012; Gao et al., 2013), and crustal compositions from analysis of P-wave velocities (Liu et al., 2006; also see Vergne et al., 2002). Northern and southern boundaries of the Qaidam-Qilian terrane, as well as a crustal boundary between the Qilian orogen and the Qaidam crust, are adapted from several recent studies on the history of terrane accretion in north China (e.g., Yin et al., 2007b; Pullen et al., 2008). The architecture of the Tertiary faults outside of our field area is adapted from structural interpretations of outcrop and seismic-reflection data, which generally indicate that the Haiyuan fault and the north-vergent thrusts of the northern Qilian Shan are part of an imbricate fan that soles into a low-angle detachment/shear zone in the middle crust (Gaudemer et al., 1995; Meyer et al., 1998; Gao et al., 2013). The architecture of Tertiary structures that are collocated with the Kunlun suture is discussed in additional detail later herein.

Our regional interpretation of the crustal architecture is generally consistent with pre-
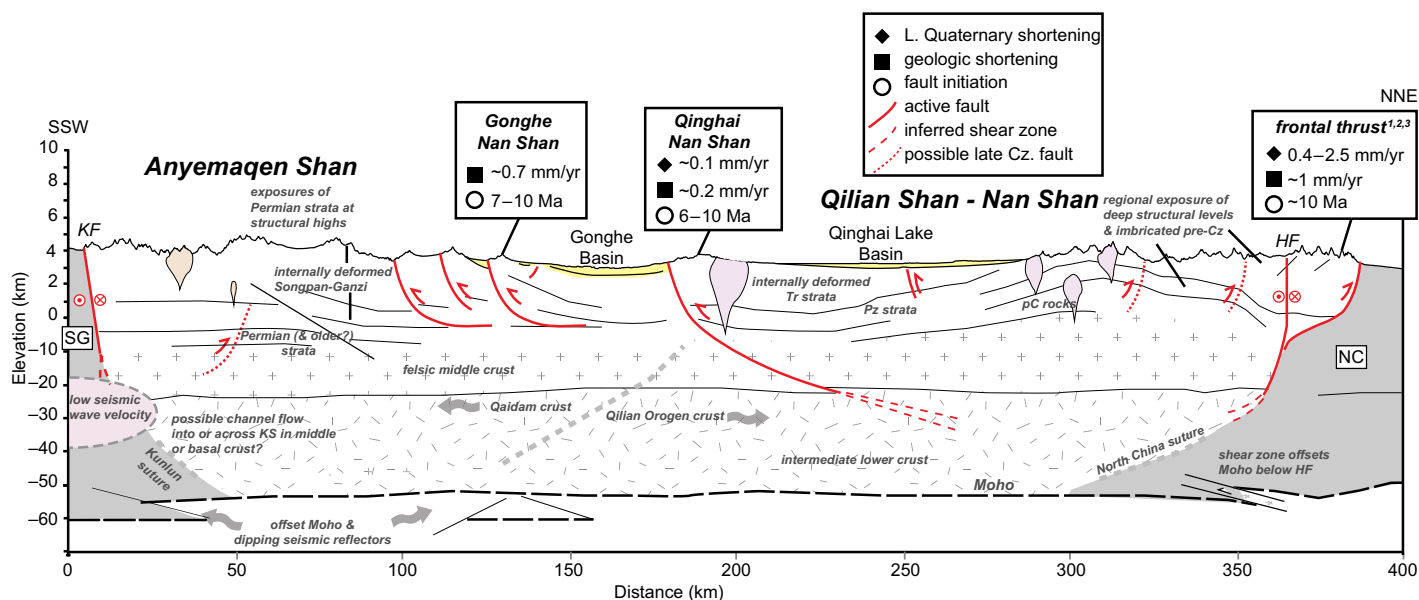
Figure 16. Interpreted crustal architecture along an approximately NNE-striking profile between the Kunlun fault and the Hexi Corridor, and transecting the Gonghe Basin complex. Fault initiation and shortening rates are similar on opposing sides of the Qilian Shan–Nan Shan, but faults verge in opposite directions. See text for more discussion. Architecture of terrane boundaries is adapted from Yin et al. (2007b) and Pullen et al. (2008). SG—Songpan-Ganzi terrane, which is separated from the Qaidam-Qilian terrane by the Kunlun suture (KS). NC—North China terrane, which is separated from the Qaidam-Qilian terrane by the North China suture. Architecture of Tertiary structures that overprint/reactivate sutures is adapted from Gaudemer et al. (1995); Meyer et al. (1998); Vergne et al. (2002); Wang et al. (2011); and Gao et al. (2013). Composition of crust is adapted primarily from Liu et al. (2006). Low-seismic-velocity zone is adapted from Yang et al. (2012). Moho depths are adapted from Vergne et al. (2002), Galvé et al. (2002), Zhang et al. (2011), and Gao et al. (2013). Slip rates and fault initiation ages are from 1—Hetzel et al. (2004); 2—Champagnac et al. (2010); and 3—Zheng et al. (2010). Tr—Triassic, Pz—Paleozoic, pC—Precambrian; Cz—Cenozoic. KF—Kunlun fault; HF—Haiyuan fault.

vious interpretations, which characterize the Qilian Shan–Nan Shan orogenic belt as a doubly vergent orogenic wedge, with the key exception being that we do not envisage that brittle faults extend into the lower crust (Burchfiel et al., 1989; Tapponnier et al., 1990, 2001; Meyer et al., 1998). We note that this cross section is bound to the east and west by the Riyueshan fault and the Elashan fault (Fig. 1; not depicted in Fig. 16), which appear to accommodate rotation of crustal blocks between the Haiyuan and Kunlun fault (e.g., Duvall and Clark, 2010).

**Shortening Budget across Gonghe Basin Complex**

Neogene shortening budgets for the Gonghe Basin of ~6–8 km on WNW-striking fault networks and ~1 km of shortening on N-S–striking fault networks (Lease et al., 2012b) are comparable to Cenozoic shortening around the Xunhua-Guide Basin (Fig. 1), indicating ~10 km of E-W crustal shortening distributed across several structures since the middle Miocene (preceded by an additional ~10 km of NNE-SSW from the middle Eocene to middle Miocene; Lease et al., 2012b). Lease et al. (2012b) deter-

mined that this relatively modest shortening is sufficient to account for modern crustal thicknesses of 56 ± 4 km without invoking thickening by channel flow in the lower crust, given a pre-Cenozoic crustal thickness of 45 ± 5 km (which is similar to stable cratonal regions adjacent to the Tibetan Plateau; see Lease et al., 2012b, and references therein). However, the assumption of 45 km pre-Cenozoic crustal thickness requires crustal recycling in an amount nearly equal to the modern orogenic volume in order to accommodate Indo-Asian crustal convergence since 40 Ma (Yakovlev and Clark, 2014). Modest Cenozoic shortening is similar to the findings of other studies focused on northern Qaidam (e.g., Yin et al., 2008a) and along the Haiyuan fault (Gao et al., 2013). Assuming a modern crustal thickness in the Gonghe region of 54 ± 6 km (Vergne et al., 2002; Galvé et al., 2002; Zhang et al., 2011; Yang et al., 2012) and an area that is 200 km in the WNW dimension by 150 km in the NNE dimension, we estimate a pre-Neogene crustal thickness of 52 +5/–7 km for the Gonghe Basin region, using the volumetric calculations and assumptions described by Lease et al. (2012b). Although this number overlaps with the estimated crustal thickness

of cratonic regions adjacent to the Tibetan Plateau, it is somewhat higher than most estimates (e.g., Liu et al., 2006; Yang et al., 2012; Lease et al., 2012b).

The small amount of crustal thickening across the Gonghe region may be reconciled with present-day crustal thicknesses in several ways. First, our shortening budget is a minimum, and it does not capture any one of several potential sources of crustal thickening. It does not capture thickening related to distributed deformation across the study area. However, relatively deep exposures of basin fill along the Yellow River canyon show that Pliocene–Quaternary strata are flat-lying across the interiors of Tongde subbasin and Gonghe Basin, such that significant distributed contractional strain is unlikely, nor does our budget capture Neogene shortening across the several ranges of modest relief (~800 m) and bounded by steep (50°–70°) reverse faults in the Elashan/Dulan–Chaka Highland region, on the southwestern flank of our study area (Duvall et al., 2013). Although shortening budgets for these ranges are not known, they are likely to be modest in light of the steep range-bounding faults and modest topographic relief (Duvall et al., 2013).

Second, it is also possible that pre-Neogene crust across the Gonghe region may have been atypically thick, such that a minimal amount of crustal thickening would be required to attain modern thicknesses (e.g., Lease et al., 2012b). Certainly, a number of studies suggest that this region has been subject to deformation beginning in Eocene time (e.g., Mock et al., 1999; Dupont-Nivet et al., 2004; Yin et al., 2007a, 2008a, 2008b; Clark et al., 2010; Duvall et al., 2011). We do not, however, find evidence for major contractional tectonism in the Gonghe region (e.g., no foreland basin). Alternatively, the presence of multiple geologic sutures (e.g., Yin et al., 2007b; Pullen et al., 2008), as well as thrust faults of generally unknown age that expose deep structural levels in the Anyemaqen Shan and Qilian Shan (GBGMR, 1989; QBGMR, 1991) suggest the possibility of significant crustal thickening prior to the Cenozoic, although budgets of such deformation remain preliminary (Craddock et al., 2011b).

Finally, it is possible that some preferential thickening of the lower crust has occurred. Indeed, interpretations of seismic-reflection experiments reveal that the lower crust below the Anyemaqen and parts of interior northeastern Tibet is intermediate in composition and anomalously thick compared to adjacent cratonal regions (e.g., Liu et al., 2006). It seems possible that thickening of the lower crust could have occurred by injection of lower-crustal material in the southern part of the study area, beneath the Anyemaqen Shan, and possibly beneath southern Gonghe Basin, where surface faults appear to be upper-crustal features. In this region, duplexing of the lower crust has been interpreted below the Anyemaqen Shan, based on Moho offsets and low-angle seismic reflectors that extend a few tens of kilometers to the north of the Kunlun fault and a possible duplicated Moho below Tongde subbasin (Zhu and Helmberger, 1998; Galvé et al., 2002; Vergne et al., 2002; see discussion in Wang et al., 2011; depicted in Fig. 16 as offset Moho). Alternatively, lateral transfer of material may have occurred above the Moho, in the lower or middle crust (e.g., Clark and Royden, 2000). A low-velocity seismic wave zone at a depth of ~20–40 km has been documented beneath the southern Anyemaqen–Qinling Shan region (Yang et al., 2012; depicted in Fig. 16). Such a zone could facilitate northward crustal flow from the plateau interior and thickening where it encounters more rigid crust beneath the Anyemaqen Shan and farther west beneath the Qaidam Basin (Clark and Royden, 2000; Kirby and Harkins, 2013). However, it is not clear to us how such a channel would interact with the Kunlun fault at depth at the latitude of ~100°E

(Fig. 16). North of the Anyemaqen Shan–southern Gonghe (latitude of ~100°E), we consider channel flow in the lower crust to be less likely if the pre-Cenozoic crust was thick (e.g., Yin et al., 2008b; Lease et al., 2012b; Gao et al., 2013).

## Kinematics and Dynamics of Faulting in Northeastern Tibet

Our results reveal that late Cenozoic shortening rates across the Qinghai Nan Shan of 0.2 +0.2/–0.1 km/m.y. overlap with late Quaternary slip rates of ~0.10 ± 0.04 mm/yr, implying relatively steady deformation across the area since the late Miocene. The assumption of steady shortening is central to recent estimates of a late Miocene initiation age for the dextral strike-slip Elashan and Riyueshan faults (Yuan et al., 2011; Lu et al., 2012), and our data bolster the validity of this assumption. Furthermore, it appears as though the major fault networks around all of the margins of the Gonghe complex initiated over a narrow time window between ca. 10 Ma and ca. 6 Ma (Craddock et al., 2011a; Yuan et al., 2011; Zhang et al., 2012; Lu et al., 2012; Yuan et al., 2013). The similar initiation age and apparently steady deformation on the WNW-striking thrusts and NNW-striking, right-lateral, strike-slip fault networks bounding Gonghe Basin imply that the presently active faults have experienced kinematically coordinated deformation for a substantial period of time during the late Cenozoic. Notably, rock uplift rates in the ranges bounding Gonghe Basin are significantly lower than apparent late Quaternary incision rates along the Yellow River (Craddock et al., 2010; Perrineau et al., 2011), reinforcing the notion that canyon incision significantly lagged range growth and filling of ponded basins in this part of the Tibetan Plateau (Craddock et al., 2010).

If the present-day rate of 4–6 mm/yr of convergence between the high plateau and the Hexi Corridor observed in geodetic data is representative of geologic rates (Gan et al., 2007; Duvall and Clark, 2010; Yuan et al., 2011), then additional shortening or strike-slip faulting must be distributed elsewhere in northeastern Tibet. Following the previous discussion, one possibility is that shortening may be distributed throughout the Anyemaqen Shan and the Elashan/Dulan–Chaka Highlands (Duvall et al., 2013), or the Anyemaqen Shan. (Note: the orientation would be orthogonal to any diffuse strain accumulation on the southern side of the fault proposed by Kirby and Harkins [2013].) Although there are narrow slivers of Cretaceous basins exposed across the Anyemaqen and the Qinling (Horton et al., 2004; Dupont-Nivet et al., 2004; Craddock et al., 2010), the region generally lacks

Cenozoic sedimentary cover to serve as structural markers. However, ongoing differential rock uplift across this range has been suggested as an explanation for spatial patterns in fluvial incision rates (Harkins et al., 2007; Kirby and Harkins, 2013), and the range itself overlies thickened crust along the Kunlun suture (e.g., Liu et al., 2006). Several active faults exist within the Anyemaqen region (depicted schematically in Fig. 16, where a possible a blind fault underlies a topographic step in the northern Anyemaqen Shan; Harkins et al., 2010; Wang et al., 2011), but the rates of shortening associated with these structures remain unknown. A final possibility is that some strain may be absorbed along faults interior to the Qilian Shan, north of Qinghai Lake; at present, however, no active faults have been recognized in this region (e.g., Hetzel, 2013).

To the north of the Anyemaqen Shan, and between 99°E–101°E, active shortening appears to be accommodated by arrays of thrust faults on opposing sides of the Qilian Shan–Nan Shan, consistent with the description of the region as a doubly vergent orogenic belt (Fig. 16; e.g., Meyer et al., 1998). As we have shown, the thrust faults along the margins of the Gonghe Basin complex appear to have absorbed 0.6–1.4 mm/yr of NNE-oriented shortening over the last 6–10 m.y. (Fig. 16). Similarly, shortening rates along the northern Qilian Shan frontal thrust, determined from deformed terraces, range from ~0.4–1.1 mm/yr (Hetzel et al., 2004) to ~2.5 mm/yr (Champagnac et al., 2010) (Fig. 16). These shortening rates agree with attendant river incision/erosion rates into uplifted fault blocks across the region (Hetzel et al., 2002; Pan et al., 2003, 2007, 2010; Zheng et al., 2010), as well as Late Tertiary rates derived from restoration of crustal-scale cross sections (Gaudemer et al., 1995). Thus, it appears that shortening rates are approximately symmetrical on opposing sides of the eastern Qilian Shan–Nan Shan ranges. In total, the geologic data permit ~2–4 mm/yr of shortening across opposing sides of the Qilian Shan, and this appears to account for most of the geodetic budget (4–6 mm/yr; Gan et al., 2007).

Notably, net shortening rates across the Qilian Shan indicated by geodetic measurements (Gan et al., 2007) and by our summation of Quaternary slip rates are significantly lower than net rates of 15 ± 5 km/m.y. obtained previously by retrodeformation of serial cross sections and by a series of mass balance considerations by Meyer et al. (1998). Although most of these authors' cross sections suggest >100 km of shortening (Meyer et al., 2998), we note that one cross section implies that the Neogene shortening budget across the Qilian Shan has

been closer to ~35–45 km. This lower estimate would be consistent with modern rates implied by geodetic measurements. Moreover, we note that the mass balance calculation presented by those authors, in which sediment from Qaidam, Gonghe, and the Hexi Corridor is restored to a Qilian Shan provenance area in order to estimate Neogene crustal thickening, is likely to be an overestimate, in light of the fact that much of the sediment in Qaidam, and perhaps in Gonghe, could have been sourced from points south (e.g., Métivier et al., 1998; Wang et al., 2006; Yin et al., 2008b; Craddock et al., 2010).

Not only do shortening rates appear to be similar on opposing sides of the Qilian Shan, but the initiation ages of major thrust faults appear to be coordinated in time. In particular, mineral cooling ages from the northeastern Qilian Shan indicate rapid cooling in this range at ca. 10 Ma (Zheng et al., 2010). The onset of thrusting in the eastern Qilian Shan is also similar in age to the onset of widespread range growth to the east and west, at ca. 8 Ma (e.g., Fang et al., 2005; Zheng et al., 2006; Lease et al., 2007; Bovet et al., 2009) and/or an acceleration in crustal shortening rates in the Guide-Xunhua region at ca. 12 Ma (Lease et al., 2012b). The similarity in both timing (10 ± 2 Ma) and rate of deformation, and the opposing vergence of faults on either flank of the Qilian Shan–Nan Shan suggest relatively rapid expansion/widening of the Qilian Shan–Nan Shan since that time of about ~150 km to the north and east (Clark, 2012; Duvall et al., 2013; Yuan et al., 2013). Such a regional episode of mountain building could be associated with an increase in topographic stress exerted by the 5-km-high plateau on its foreland (England and Houseman, 1986; Houseman and England, 1986; Tapponnier et al., 1990, 2001), possibly transmitted by the relatively rigid Qaidam Basin (e.g., Dupont-Nivet et al., 2002; Dayem et al., 2009; Zheng et al., 2010). Alternatively, this episode could relate to the onset of regional-scale transpression during the later stages of orogenesis that followed progressive confinement of Tibet against rigid blocks to the north and expansion of crustal thickening by lower-crustal flow to the east (Duvall et al., 2013).

## CONCLUSIONS

New geologic data place bounds on the style, magnitude, and rates of upper-crustal shortening across the interior of the northeastern Tibetan Plateau and lead us to arrive at the following conclusions.

(1) Structural, geomorphic, and thermochronologic markers provide the basis for detailed analysis of the two S-vergent networks of imbricate thrust faults along the margins of the Gonghe Basin complex, the Qinghai Nan Shan and the Gonghe Nan Shan. The Qinghai Nan Shan has accommodated ~0.8–2.2 km of upper-crustal shortening since the late Miocene, and the Gonghe Nan Shan has accommodated ~5.1–6.9 km over a similar time frame.

(2) When integrated with previous stratigraphic studies of the timing of deformation along the margins of Gonghe Basin (Craddock et al., 2011a; Zhang et al., 2012), average geologic shortening rates across the Qinghai Nan Shan appear to be 0.2 +0.2/–0.1 km/m.y., and rates across the Gonghe Nan Shan appear to be ~0.7 +0.3/–0.2 km/m.y.

(3) Dating and restoration of a deformed alluvial-fan surface along the SW front of the Qinghai Nan Shan indicate that late Quaternary shortening rates are 0.10 ± 0.04 mm/yr. These rates are relatively slow, and they overlap with average late Cenozoic shortening rates across the range.

(4) The structural architecture of the Qinghai and Gonghe Nan Shan fault systems suggests that they sole into décollements in the upper or middle crust. The décollement depth for the Qinghai Nan Shan appears to be at least ~30 km, whereas the décollement depth beneath the Gonghe Nan Shan is shallower, between ~7 and 9 km.

(5) The correspondence between post–late Miocene slip rates and late Quaternary slip rates suggests relatively steady deformation since the late Miocene across the northeastern Tibetan Plateau. Slow, steady shortening on S-vergent fault networks along the Gonghe Basin is mirrored by slow, steady N-vergent thrusting along the northern Qilian Shan front range. Both fault systems appear to have initiated between 7 and 10 Ma and imply that the doubly vergent Qilian Shan–Nan Shan orogeny has expanded outward since the late Miocene.

## APPENDIX

### Cosmogenic Isotope Dating Methods

Samples were subjected to several physical and chemical treatments designed to purify the raw material to pure quartz. First, samples were crushed and sieved to 250–500 μm for the remaining treatments. In order to remove carbonates and minor metals, the crushed material was leached in nitric acid and aqua regia. Next, the sample was subjected to a suite of physical separation steps, including: froth flotation, magnetic separation, a purification bath in a hydrofluoric acid–nitric acid solution, and heavy liquid separation. The remaining material was soaked for a second time in a hydrofluoric acid–nitric acid solution to remove any remaining feldspars. During this step, the outermost layers of the quartz grains were dissolved to remove meteoric [10]Be. After completing this routine, Al concentrations were measured on an inductively coupled plasma–optical emissions spectrometer (ICP-OES) to assess the purity of the remaining quartz. If the measured Al concentration (which signifies the presence of residual feldspars) exceeded 200 ppm, the final step was repeated as necessary.

In order to extract Be isotopes from the purified quartz samples, a second series of chemical treatments was applied. After adding Be carriers, quartz was dissolved in concentrated hydrofluoric acid. The volume of the solution containing the dissolved sample was reduced, and the hydrofluoric acid was removed by a series of evaporation and fuming steps. The residual material was taken up in a sodium hydroxide solution, centrifuged, and decanted in order to separate Fe and Ti ions from the solid residual sample. Next, the pH of the remaining solution was adjusted to ~8 to precipitate the Be out of the solution as hydroxides (Ochs and Ivy-Ochs, 1997). After dissolving the remaining hydroxides in oxalic acid, cation and anion columns were used to removed residual Na, Fe, and other undesired ions, and to isolate Be. The samples were dried and fired in an oven, and then loaded into a cathode for accelerator mass spectrometry (AMS). AMS was conducted at the PRIME Laboratory at Purdue University, following standard protocols.

## REFERENCES CITED

Amos, C.B., Burbank, D.W., Nobes, D.C., and Read, S.A., 2007, Geomorphic constraints on listric thrust faulting: Implications for active deformation in the Mackenzie Basin, South Island, New Zealand: Journal of Geophysical Research, v. 112, B03S11, 24 p., doi:10.1029/2006JB004291.

An, Z., Wang, P., Shen, J., Zhang, Y.X., Zhang, P.Z., Wang, S.M., Li, X.Q., Sun, Q.L., Song, Y.G., Ai, L., Zhang, Y.C., Jiang, S.R., Liu, X.Q., and Wang, Y., 2006, Geophysical survey on the tectonic and sediment distribution of Qinghai Lake basin: Science in China, ser. D, v. 49, p. 851–861, doi:10.1007/s11430-006-0851-1.

Anderson, R.S., Repka, J.L., and Dick, G.S., 1996, Explicit treatment of inheritance in dating depositional surfaces using in situ [10]Be and [26]Al: Geology, v. 24, no. 1, p. 47–51, doi:10.1130/0091-7613(1996)024<0047:ETOIID>2.3.CO;2.

Avouac, J.-P., and Tapponnier, P., 1993, Kinematic model of active deformation in central Asia: Geophysical Research Letters, v. 20, no. 10, p. 895–898, doi:10.1029/93GL00128.

Bovet, P.M., Ritts, B.D., Gehrels, G., Abbink, A.O., Darby, B.J., and Hourigan, J., 2009, Evidence of Miocene

crustal shortening in the North Qilian Shan from Cenozoic stratigraphy of the western Hexi Corridor, Gansu Province, China: American Journal of Science, v. 309, p. 290–329, doi:10.2475/00.4009.02.

Bullen, M.E., Burbank, D.W., and Garver, J.I., 2003, Building the northern Tien Shan: Integrated thermal, structural, and topographic constraints: The Journal of Geology, v. 111, no. 2, p. 149–165, doi:10.1086/345840.

Burchfiel, B.C., Deng, Q., Molnar, P., Royden, L.H., Wang, Y., Zhang, P., and Zhang, W., 1989, Intracrustal detachment within zones of continental deformation: Geology, v. 17, p. 748–752, doi:10.1130/0091-7613(1989)017<0448:IDWZOC>2.3.CO;2.

Burchfiel, B.C., Royden, L.H., van der Hilst, R.D., Hager, B.H., Chen, Z., King, R.W., Li, C., Lu, J., Yao, H., and Kirby, E., 2008, A geological and geophysical context for the Wenchuan earthquake of 12 May 2008, Sichuan, People's Republic of China: GSA Today, v. 18, no. 7, p. 4, doi:10.1130/GSATG18A.1.

Burtner, R.L., Nigrinin, A., and Donelick, R.A., 1994, Thermochronology of Lower Cretaceous source rocks in the Idaho-Wyoming thrust belt: American Association of Petroleum Geologists Bulletin, v. 78, p. 191–199.

Candy, I., Black, S., and Sellwood, B.W., 2004, Quantifying time scales of pedogenic calcrete formation using U-series disequilibria: Sedimentary Geology, v. 170, no. 3/4, p. 177–187, doi:10.1016/j.sedgeo.2004.07.003.

Carlson, W.D., Donelick, R.A., and Ketcham, R.A., 1999, Variability of apatite fission-track annealing kinetics: 1. Experimental results: The American Mineralogist, v. 84, p. 1213–1223.

Cerling, T.E., and Craig, H., 1994, Geomorphology and in-situ cosmogenic isotopes: Annual Review of Earth and Planetary Sciences, v. 22, p. 273–317, doi:10.1146/annurev.ea.22.050194.001421.

Champagnac, J.D., Yuan, D.Y., Ge, W.P., Molnar, P., and Zheng, W.J., 2010, Slip rate at the north eastern front of the Qilian Shan, China: Terra Nova, v. 22, no. 3, p. 180–187, doi:10.1111/j.1365-3121.2010.00932.x.

Chen, Y.T., and Xu, L.S., 2000, A time-domain inversion technique for the tempo-spatial distribution of slip on a finite fault plane with applications to recent large earthquakes in the Tibetan Plateau: Geophysical Journal International, v. 143, no. 2, p. 407–416, doi:10.1046/j.1365-246X.2000.01263.x.

Chen, Y.T., Xu, L.S., Li, X., and Zhao, M., 1996, Source process of the 1990 Gonghe, China, earthquake and tectonic stress field in the northeastern Qinghai-Zixang (Tibetan) Plateau: Pure and Applied Geophysics, v. 146, p. 697–715, doi:10.1007/BF00874741.

Clark, M.K., 2012, Continental collision slowing due to viscous mantle lithosphere rather than topography: Nature, v. 483, p. 74–77, doi:10.1038/nature10848.

Clark, M.K., and Bilham, R., 2008, Miocene rise of the Shillong Plateau and the beginning of the end for the Eastern Himalaya: Earth and Planetary Science Letters, v. 269, p. 337–351, doi:10.1016/j.epsl.2008.01.045.

Clark, M.K., and Royden, L.H., 2000, Topographic ooze: Building the eastern margin of Tibet by lower crustal flow: Geology, v. 28, no. 8, p. 703–706, doi:10.1130/0091-7613(2000)28,703:TOBTEM>2.0.CO;2.

Clark, M.K., Farley, K.A., Zheng, D., and Duvall, A.R., 2010, Early Cenozoic faulting of the northern Tibetan Plateau margin from apatite (U-Th)/He ages: Earth and Planetary Science Letters, v. 296, no. 1–2, p. 78–88, doi:10.1016/j.epsl.2010.04.051.

Cowie, P.A., Sornette, D., and Vanneste, C., 1995, Multifractal scaling properties of a growing fault population: Geophysical Journal International, v. 122, no. 2, p. 457–469, doi:10.1111/j.1365-246X.1995.tb07007.x.

Craddock, W.H., Kirby, E., Harkins, N., Zhang, H., Shi, X., and Liu, J., 2010, Rapid fluvial incision along the Yellow River during headward basin integration: Nature Geoscience, v. 3, p. 209–213, doi:10.1038/ngeo777.

Craddock, W.H., Kirby, E., and Zhang, H., 2011a, Late Miocene–Pliocene range growth in the interior of the northeastern Tibetan Plateau: Lithosphere, v. 3, no. 6, p. 420–438, doi:10.1130/L159.1.

Craddock, W.H., Kirby, E., Zheng, D., and Liu, J., 2011b, Tectonic setting of Cretaceous basins on the NE Tibetan Plateau: Insights from the Jungong Basin:

Basin Research, v. 24, no. 1, p. 51–69, doi:10.1111/j.1365-2117.2011.00515.x.

Dayem, K.E., Molnar, P., Clark, M.K., and Houseman, G.A., 2009, Far-field lithospheric deformation in Tibet during continental collision: Tectonics, v. 28, TC6005, doi:10.1029/2008TC002344.

Dolan, J.F., Bowman, D.D., and Sammis, C.G., 2007, Long-range and long-term fault interactions in southern California: Geology, v. 35, no. 9, p. 855–858, doi:10.1130/G23789A.1.

Donelick, R.A., O'Sullivan, P.B., and Ketcham, R.A., 2005, Apatite fission-track analysis: Reviews in Mineralogy and Geochemistry, v. 58, no. 1, p. 49–94, doi:10.2138/rmg.2005.58.3.

Dragert, H., Wang, K., and James, T.S., 2001, A silent slip event on the deeper Cascadia subduction interface: Science, v. 292, no. 5521, p. 1525–1528, doi:10.1126/science.1060152.

Dubey, A.K., and Cobbold, P.R., 1977, Noncylindrical flexural slip folds in nature and experiment: Tectonophysics, v. 38, no. 3, p. 223–239, doi:10.1016/0040-1951(77)90212-8.

Dupont-Nivet, G., Butler, R.F., Yin, A., and Chen, X., 2002, Paleomagnetism indicates no Neogene rotation of the Qaidam Basin in northern Tibet during Indo-Asian collision: Geology, v. 30, no. 3, p. 263–266, doi:10.1130/0091-7613(2002)030<0263:PINNRO>2.0.CO;2.

Dupont-Nivet, G., Horton, B.K., Butler, R.F., Wang, B., Zhou, J., and Waanders, G.L., 2004, Paleogene clockwise tectonic rotation of the Xining-Lanzhou region, northeastern Tibetan Plateau: Journal of Geophysical Research, v. 109, B04401, doi:10.1029/2003JB002620.

Duvall, A.R., and Clark, M.K., 2010, Dissipation of fast strike-slip faulting within and beyond northeastern Tibet: Geology, v. 88, no. 8, p. 223–226, doi:10.1130/G30711.1.

Duvall, A.R., Clark, M.K., van der Pluijm, B.A., and Li, C., 2011, Direct dating of Eocene reverse faulting in northeastern Tibet using Ar-dating of fault clays and low-temperature thermochronometry: Earth and Planetary Science Letters, v. 304, no. 3–4, p. 520–526, doi:10.1016/j.epsl.2011.02.028.

Duvall, A.R., Clark, M.K., Kirby, E., Farley, K.A., Craddock, W.H., Li, C., and Yuan, D.-Y., 2013, Low-temperature thermochronometry along the Kunlun and Haiyuan faults, NE Tibetan Plateau: Evidence for kinematic change during late-stage orogenesis: Tectonics, v. 32, no. 5, p. 1190–1211, doi:10.1002/tect.20072.

England, P., and Houseman, G.A., 1986, Finite strain calculations of continental deformation: 2. Comparison with the India-Asia collision zone: Journal of Geophysical Research, v. 91, no. B3, p. 3664–3676, doi:10.1029/JB091iB03p03664.

England, P., and Jackson, J., 2011, Uncharted seismic risk: Nature Geoscience, v. 4, no. 6, p. 348–349, doi:10.1038/ngeo1168.

Erdős, Z., van der Beek, P., and Huismans, R.S., 2014, Evaluating balanced section restoration with thermochronology data: A case study from the central Pyrenees: Tectonics, v. 33, no. 5, p. 617–634, doi:10.1002/2013TC003481.

Fang, X., Yan, M., Van der Voo, R., Rea, D.K., Song, C., Pares, J.M., Gao, J., Nie, J., and Dai, S., 2005, Late Cenozoic deformation and uplift of the NE Tibetan Plateau: Evidence from high-resolution magnetostratigraphy of the Guide Basin, Qinghai Province, China: Geological Society of America Bulletin, v. 117, no. 9–10, p. 1208–1225, doi:10.1130/B25727.1.

Fang, X., Zhang, W., Meng, Q., Gao, J., Wang, X., King, J., Song, C., Dai, S., and Miao, Y., 2007, High-resolution magnetostratigraphy of the Neogene Huaitoutala section in the eastern Qaidam Basin on the NE Tibetan Plateau, Qinghai Province, China, and its implications on the tectonic uplift of the NE Tibetan Plateau: Earth and Planetary Science Letters, v. 258, no. 1–2, p. 293–306, doi:10.1016/j.epsl.2007.03.042.

Farley, K.A., 2002, (U-Th)/He dating: Techniques, calibrations, and applications: Reviews in Mineralogy and Geochemistry, v. 47, no. 1, p. 819–844, doi:10.2138/rmg.2002.47.18.

Flowers, R.M., Ketcham, R.A., Shuster, D.L., and Farley, K.A., 2009, Apatite (U-Th)/He thermochronometry

using a radiation damage accumulation and annealing model: Geochimica et Cosmochimica Acta, v. 73, no. 8, p. 2347–2365, doi:10.1016/j.gca.2009.01.015.

Galbraith, R.F., 2005, Statistics for Fission Track Analysis: Boca Raton, Florida, Chapman and Hall/CRC, 229 p.

Galvé, A., Hirn, A., Jiang, M., Gallart, J., de Voodg, B., LéPine, J.-C., Diaz, J., Wang, Y., and Qian, H., 2002, Modes of raising northeastern Tibet probed by explosion seismology: Earth and Planetary Science Letters, v. 203, no. 1, p. 35–43, doi:10.1016/S0012-821X(02)00863-4.

Gan, W., Zhang, P., Shen, Z.K., Niu, Z., Wang, M., Wan., Y., and Cheng, J., 2007, Present-day crustal motion within the Tibetan Plateau inferred from GPS measurements: Journal of Geophysical Research, v. 112, B08416, 14 p., doi:10.1029/2005JB004120.

Gansu Bureau of Geology and Mineral Resources (GBGMR), 1989, Regional Geology of Gansu Province: Beijing, Geological Publishing House, 690 p., scale 1:200,000.

Gao, R., Wang, H., Yin, A., Dong, S., Kuang, Z., Zuza, A.V., Li, W., and Xiong, X., 2013, Tectonic development of the northeastern Tibetan Plateau as constrained by high-resolution deep seismic reflection data: Lithosphere, v. 5, no. 6, p. 555–574, doi:10.1130/L293.1.

Gaudemer, Y., Tapponnier, P., Meyer, B., Peltzer, G., Guo, S., Chen, Z., Dai, H., and Cifuentes, I., 1995, Partitioning of crustal slip between linked active faults in the eastern Qilian Shan, and evidence for a major seismic gap, the "Tianzhu gap," on the western Haiyuan fault, Gansu (China): Geophysical Journal International, v. 120, no. 3, p. 599–645, doi:10.1111/j.1365-246x.1995.tb01842.x.

Gehrels, G.E., Yin, A., and Wang, X.F., 2003, Detrital-zircon geochronology of the northeastern Tibetan Plateau: Geological Society of America Bulletin, v. 115, no. 7, p. 881–896, doi:10.1130/0016-7606(2003)115<0881:DGOTNT>2.0.CO;2.

Global Centroid Moment Tensor Catalog, 2012, Global Centroid Moment Tensor Catalog: http://www.globalcmt.org/ (accessed 1 December 2012).

Gosse, J.C., and Phillips, F.M., 2001, Terrestrial in situ cosmogenic nuclides: Theory and application: Quaternary Science Reviews, v. 20, no. 14, p. 1475–1560, doi:10.1016/S0277-3791(00)00171-2.

Hancock, G.S., Anderson, R.S., Chadwick, O.A., and Finkel, R.C., 1999, Dating fluvial terraces with [10]Be and [26]Al profiles: Application to the Wind River, Wyoming: Geomorphology, v. 27, no. 1/2, p. 41–60, doi:10.1016/S0169-555X(98)00089-0.

Hao, M., Shen, Z.K., Wang, Q., and Cui, D., 2012, Postseismic deformation mechanisms of the 1990 Mw 6.4 Gonghe, China, earthquake constrained using line leveling measurements: Tectonophysics, v. 532–535, p. 205–214, doi:10.1016/j.tecto.2012.02.005.

Harkins, N., Kirby, E., Heimsath, A., Robinson, R., and Reiser, U., 2007, Transient fluvial incision in the headwaters of the Yellow River, northeastern Tibet, China: Journal of Geophysical Research, v. 112, F03S04, doi:10.1029/2006JF000570.

Harkins, N., Kirby, E., Shi, X., Wang, E., Burbank, D.W., and Chun, F., 2010, Millennial slip rates along the eastern Kunlun fault: Implications for the dynamics of intracontinental deformation in Asia: Lithosphere, v. 2, no. 4, p. 247–266, doi:10.1130/L85.1.

Hasebe, N., Barbarand, J., Jarvis, K., Carter, A., and Hurford, A.J., 2004, Apatite fission-track chronometry using laser ablation ICP-MS: Chemical Geology, v. 207, no. 3–4, p. 135–145, doi:10.1016/j.chemgeo.2004.01.007.

Hetzel, R., 2013, Active faulting, mountain growth, and erosion at the margins of the Tibetan Plateau constrained by in situ–produced cosmogenic nuclides: Tectonophysics, v. 582, p. 1–24, doi:10.1016/j.tecto.2012.10.027.

Hetzel, R., and Hampel, A., 2005, Slip rate variations on normal faults during glacial-interglacial changes in surface loads: Nature, v. 435, p. 81–84, doi:10.1038/nature03562.

Hetzel, R., Niedermann, S., Tao, M., Kubik, P.W., Ivy-Ochs, S., Gao, B., and Strecker, M.R., 2002, Low slip rates and long-term preservation of geomorphic features in

central Asia: Nature, v. 417, p. 428–432, doi:10.1038 /417428a.

Hetzel, R., Tao, M., Stokes, S., Nidermann, S., Ivy-Ochs, S., Gao, B., Strecker, M.R., and Kubik, P.W., 2004, Late Pleistocene/Holocene slip rate of the Zhangye thrust (Qilian Shan, China) and implications for the active growth of the northeastern Tibetan Plateau: Tectonics, v. 23, TC6006, 17 p., doi:10.1029/2004TC001653.

Hidy, A.J, Gosse, J.C., Pederson, J.L., Mattern, J.P., and Finkel, R.C., 2010, A geologically constrained Monte Carlo approach to modeling exposure ages from profiles of cosmogenic nuclides: An example from Lees Ferry, Arizona: Geochemistry, Geophysics, Geosystems, v. 11, Q0AA10, 18 p., doi:10.1029/2010GC003084.

Horton, B.K., Dupont-Nivet, G., Zhou, J., Waanders, G.L., Butler, R.F., and Wang, J., 2004, Mesozoic–Cenozoic evolution of the Xining-Minhe and Dangchang Basins, northeastern Tibetan Plateau: Magnetostratigraphic and biostratigraphic results: Journal of Geophysical Research, v. 109, B04402, doi:10.1029/2003JB002913.

Hough, B.G., Garzione, C.N., Wang, Z., Lease, R.O., Burbank, D.W., and Yuan, D., 2011, Stable isotope evidence for topographic growth and basin segmentation: Implications for the evolution of the NE Tibetan Plateau: Geological Society of America Bulletin, v. 123, no. 1–2, p. 168–185, doi:10.1130/B30090.1.

Houseman, G., and England, P., 1986, Finite strain calculations of continental deformation: 1. Method and general results for convergent zones: Journal of Geophysical Research–Solid Earth, v. 91, no. B3, p. 3651–3663, doi:10.1029/JB091iB03p03651.

Jiang, M., Galvé, A., Hirn, A., de Voogd, B., Laigle, M., Su, H.P., Diaz, J., Lépine, J.C., and Wang, X.Y., 2006, Crustal thickening and variations in architecture from the Qaidam Basin to the Qang Tang (north-central Tibetan Plateau) from wide-angle reflection seismology: Tectonophysics, v. 412, no. 3–4, p. 121–140, doi:10.1016/j.tecto.2005.09.011.

Jordan, T.A., and Watts, A.B., 2005, Gravity anomalies, flexure and the elastic thickness structure of the India–Eurasia collisional system: Earth and Planetary Science Letters, v. 236, no. 3, p. 732–750, doi:10.1016/j.epsl.2005.05.036.

Ketcham, R.A., 2005, Forward and inverse modeling of low-temperature thermochronometry data: Reviews in Mineralogy and Geochemistry, v. 58, no. 1, p. 275–314, doi:10.2138/rmg.2005.58.11.

Ketcham, R.A., Donelick, F.A., and Carlson, W.D., 1999, Variability of apatite fission-track annealing kinetics: III. Extrapolation to geological time scales: American Mineralogist, v. 84, p. 1235–1255.

Ketcham, R.A., Carter, A., Donelick, R.A., Barbarand, J., and Hurford, A.J., 2007a, Improved measurement of fission-track annealing in apatite using *c*-axis projection: The American Mineralogist, v. 92, no. 5–6, p. 789–798, doi:10.2138/am.2007.2280.

Ketcham, R.A., Carter, A., Donelick, R.A., Barbarand, J., and Hurford, A.J., 2007b, Improved modeling of fission-track annealing in apatite: American Mineralogist, v. 92, no. 5–6, p. 799–810, doi:10.2138/am.2007.2281.

Ketcham, R.A., Gautheron, C., and Tassan-Got, L., 2011, Accounting for long alpha-particle stopping distances in (U-Th-Sm)/He geochronology: Refinement of the baseline case: Geochimica et Cosmochimica Acta, v. 75, p. 7779–7791, doi:10.1016/j.gca.2011.10.011.

Kirby, E., and Harkins, N., 2013, Distributed deformation around the eastern tip of the Kunlun fault: International Journal of Earth Sciences, p. 1–14, doi:10.1007/s00531 -013-0872-x.

Kirby, E., Harkins, N., Wang, E., Shi, X., Fan, C., and Burbank, D., 2007, Slip rate gradients along the eastern Kunlun fault: Tectonics, v. 26, TC2010, 16 p., doi:10 .1029/2006TC002033.

Klemperer, S.L., 2006, Crustal flow in Tibet: Geophysical evidence for the physical state of Tibetan lithosphere, and inferred patterns of active flow, *in* Law, R.D., Searle, M.P., and Godin, L., eds., Channel Flow, Ductile Extrusion, and Exhumation in Continental Collision Zones: Geological Society of London Special Publication 268, p. 39–70, doi:10.1144/GSL.SP.2006.268.01.03.

Lease, R.O., Burbank, D.W., Gehrels, G., Wang, Z., and Yuan, D., 2007, Signatures of mountain building: Detrital

zircon U/Pb ages from northeastern Tibet: Geology, v. 35, no. 3, p. 239–242, doi:10.1130/G23057A.1.

Lease, R.O., Burbank, D.W., Hough, B., Wang, Z., and Yuan, D., 2012a, Pulsed Miocene range growth in northeastern Tibet: Insights from Xunhua Basin magnetostratigraphy: Geological Society of America Bulletin, v. 124, no. 5–6, p. 657–677, doi:10.1130/B30524.1.

Lease, R.O., Burbank, D.W., Zhang, H.P., Liu, J., and Yuan, D., 2012b, Cenozoic shortening budget for the northeastern edge of the Tibetan Plateau: Is lower crustal flow necessary?: Tectonics, v. 31, no. 3, 16 p., doi:10 .1029/2011TC003066.

Liu, M., Mooney, W.D., Li, S., Okaya, N., and Detweiler, S., 2006, Crustal structure of the northeastern margin of the Tibetan Plateau from the Songpan-Ganzi terrane to the Ordos Basin: Tectonophysics, v. 420, p. 253–266, doi:10.1016/j.tecto.2006.01.025.

Liu, Z., Wang, C., and Yi, H., 2001, Evolution and mass accumulation of the Cenozoic Hoh Xil Basin, northern Tibet: Journal of Sedimentary Research, v. 71, no. 6, p. 971–984, doi:10.1306/030901710971.

Loveless, J.P., and Meade, B.J., 2011, Partitioning of localized and diffuse deformation in the Tibetan Plateau from joint inversions of geologic and geodetic observations: Earth and Planetary Science Letters, v. 303, no. 1/2, p. 11–24, doi:10.1016/j.epsl.2010.12.014.

Lu, H., Wang, E., Shi, X., and Meng, K., 2012, Cenozoic tectonic evolution of the Elashan range and its surroundings, northern Tibetan Plateau, as constrained by paleomagnetism and apatite fission track analyses: Tectonophysics, v. 580, p. 150–161, doi:10.1016/j .tecto.2012.09.013.

Ludwig, K.R., and Paces, J.B., 2002, Uranium-series dating of pedogenic silica and carbonate, Crater Flat, Nevada: Geochimica et Cosmochimica Acta, v. 66, no. 3, p. 487–506, doi:10.1016/S0016-7037(01)00786-4.

McPhillips, D., and Brandon, M.T., 2010, Using tracer thermochronology to measure modern relief change in the Sierra Nevada, California: Earth and Planetary Science Letters, v. 296, p. 373–383, doi:10.1016/j.epsl .2010.05.022.

Métivier, F., Gaudemer, I, Tapponnier, P., and Meyer, B., 1998, Northeastward growth of the Tibet Plateau deduced from balanced reconstruction of two depositional areas: The Qaidam and Hexi Corridor basins, China: Tectonics, v. 17, no. 6, p. 823–842, doi:10.1029 /98TC02764.

Meyer, B., Tapponnier, P., Bourjot, L., Métivier, F., Gaudemer, Y., Peltzer, G., Shunmin, G., and Zhitai, C., 1998, Crustal thickening in Gansu-Qinghai, lithospheric mantle subduction, and oblique, strike-slip controlled growth of the Tibet Plateau: Geophysical Journal International, v. 135, no. 1, p. 1–47, doi:10 .1046/j.1365-246X.1998.00567.x.

Mock, C., Arnaud, N.O., and Cantagrel, J.-M., 1999, An early unroofing in northeastern Tibet? Constraints from $^{40}Ar/^{39}Ar$ thermochronology on granitoids from the eastern Kunlun range (Qianghai, NW China): Earth and Planetary Science Letters, v. 171, p. 107–122, doi: 10.1016/S0012-821X(99)00133-8.

Molnar, P., and Tapponnier, P., 1978, Active tectonics of Tibet: Journal of Geophysical Research, v. 83, no. B11, p. 5361–5375, doi:10.1029/JB083iB11p05361.

Nishiizumi, K., Imamura, M., and Caffee, M.W., 2007, Absolute calibration of $^{10}Be$ AMS standards: Nuclear Instruments & Methods in Physics Research, ser. B, Beam Interactions with Materials and Atoms, v. 258, no. 2, p. 403–413, doi:10.1016/j.nimb.2007.01.297.

Ochs, M., and Ivy-Ochs, S., 1997, The chemical behavior of Be, Al, Fe, Ca, and Mg during AMS target preparation from terrestrial silicates modeled with chemical speciation calculations: Nuclear Instruments & Methods in Physics Research, ser. B, Beam Interactions with Materials and Atoms, v. 123, no. 1–4, p. 235–240, doi: 10.1016/S0168-583X(96)00680-5.

Oskin, M., Perg, L., Shelef, E., Strane, M., Gurney, E., Singer, B., and Zhang, X., 2008, Elevated shear zone loading rate during an earthquake cluster in eastern California: Geology, v. 36, no. 6, p. 507–510, doi:10 .1130/G24814A.1.

Pan, B., Burbank, D., Wang, Y., Wu, G., Li, J., and Guan, Q., 2003, A 900 ky record of strath terrace formation

during glacial-interglacial transitions in northwest China: Geology, v. 31, no. 11, p. 957–960, doi:10.1130 /G19685.1.

Pan, B.T., Pan, H.S., Gao, G.J., Wu, J.J., Li, B.Y., Li, Y., and Ye, Y.G., 2007, Dating of erosion surface and terraces in the eastern Qilian Shan, northwest China: Earth Surface Processes and Landforms, v. 32, no. 1, p. 143–154, doi:10.1002/esp.1390.

Pan, B.T., Geng, H.P., Ju, X.F., Sun, R.H., and Wang, C., 2010, The topographic controls on the decadal-scale erosion rates in Qilian Shan mountains, NW China: Earth and Planetary Science Letters, v. 292, no. 1, p. 148–157, doi:10.1016/j.epsl.2010.01.030.

Peltzer, G., Tapponnier, P., Gaudemer, Y., Meyer, B., Guo, S., Yin, K., Chen, Z., and Dai, H., 1988, Offsets of late Quaternary morphology, rate of slip, and recurrence of large earthquakes on the Chang Ma fault (Gansu, China): Journal of Geophysical Research, v. 93, no. B7, p. 7793–7812, doi:10.1029/JB093iB07p07793.

Perrineau, A., van der Woerd, J., Gaudemer, Y., Jing, L.Z., Pik, R., Tapponnier, P., Thuizat, R., and Zheng, R., 2011, Incision rate of the Yellow River in northeastern Tibet constrained by $^{10}Be$ and $^{26}Al$ cosmogenic isotope dating of fluvial terraces: Implications for catchment evolution and plateau building, *in* Gloaguen, R., and Ratschbacher, L., eds., Growth and Collapse of the Tibetan Plateau: Geological Society of London Special Publication 353, p. 189–219, doi:10.1144/SP353.10.

Pullen, A., Kapp, P., Gehrels, G.E., Vervoort, J.D., and Ding, L., 2008, Triassic continental subduction in central Tibet and Mediterranean-style closure of the Paleo-Tethys Ocean: Geology, v. 36, no. 5, p. 351–354, doi: 10.1130/G24435A.1.

Qinghai Bureau of Geology and Mineral Resources (QBGMR), 1991, Regional Geology of Qinghai Province: Beijing, Geological Publishing House, 662 p., scale 1:200,000.

Reiners, P.W., and Brandon, M.T., 2006, Using thermochronology to understand orogenic erosion: Annual Review of Earth and Planetary Sciences, v. 34, p. 419–466, doi: 10.1146/annurev.earth.34.031405.125202.

Rockwell, T.K., Lindvall, S., Helzberg, M., Murbach, D., Dawson, T., and Berger, G., 2000, Paleoseismology of the Johnson Valley, Kickapoo, and Homestead Valley faults: Clustering of earthquake in the Eastern California shear zone: Bulletin of the Seismological Society of America, v. 90, no. 5, p. 1200–1236, doi:10.1785 /0119990023.

Rockwell, T.K., Barka, A., Dawson, T., Akyuz, S., and Thorup, K., 2001, Paleoseismology of the Gazikoy-Saros segment of the North Anatolia fault, northwestern Turkey: Comparison of the historical and paleoseismic records, implications of regional seismic hazard and models of earthquake recurrence: Journal of Seismology, v. 5, no. 3, p. 433–448, doi:10.1023/A: 1011435927983.

Roger, F., Malavieille, J., Leloup, P.H., Calassou, S., and Xu, Z., 2004, Timing of granite emplacement and cooling in the Songpan-Ganzi fold belt (eastern Tibetan Plateau) with tectonic implications: Journal of Asian Earth Sciences, v. 22, no. 5, p. 465–481, doi:10.1016/S1367 -9120(03)00089-0.

Şengör, A.M.C., and Natal'in, B.A., 1996, Paleotectonics of Asia: Fragments of a synthesis, *in* Yin, A., and Harrison, T.M., eds., The Tectonic Evolution of Asia: New York, Cambridge University Press, p. 486–640.

Shuster, D.L., Flowers, R.M., and Farley, K.A., 2006, The influence of natural radiation damage on helium diffusion kinetics in apatite: Earth and Planetary Science Letters, v. 249, no. 3–4, p. 148–161, doi:10.1016/j.epsl .2006.07.028.

Stone, J.O., 2000, Air pressure and cosmogenic isotope production: Journal of Geophysical Research–Solid Earth, v. 105, no. B10, p. 23,753–23,759, doi:10.1029 /2000JB900181.

Suppe, J., 1983, Geometry and kinematics of fault-bend folding: American Journal of Science, v. 283, no. 7, p. 684–721, doi:10.2475/ajs.283.7.684.

Tapponnier, P., and Molnar, P., 1977, Active faulting and tectonics of China: Journal of Geophysical Research, v. 82, no. 20, p. 2905–2930, doi:10.1029 /JB082i020p02905.

Tapponnier, P., Meyer, B., Avouac, J.P., Peltzer, G., Gaudemer, Y., Guo, S., Xiang, H., Yin, K., Chen, Z., Cai, S., and Dai, H., 1990, Active thrusting and folding in the Qilian Shan, and decoupling between upper crust and mantle in northeastern Tibet: Earth and Planetary Science Letters, v. 97, no. 3–4, p. 382–383, 387–403, doi:10.1016/0012-821X(90)90053-Z.

Tapponnier, P., Zhiqin, X., Roger, F., Meyer, B., Arnaud, N., Wittlinger, G., and Yang, J., 2001, Oblique stepwise rise and growth of the Tibet Plateau: Science, v. 294, no. 5547, p. 1671–1677, doi:10.1126/science.105978.

Thompson, S.C., Weldon, R.J., Rubin, C.M., Abdrakhmatov, K., Molnar, P., and Berger, G.W., 2002, Late Quaternary slip rates across the central Tien Shan, Kyrgyzstan, central Asia: Journal of Geophysical Research–Solid Earth, v. 107, no. B9, 32 p., doi:10.1029/2001JB000596.

Van der Woerd, J., Ryerson, F.J., Tapponnier, P., Meriaux, A.-S., Gaudemer, Y., Finkel, R.C., Caffee, M.W., Zhao, G., and Xu, Z., 2000, Uniform slip-rate along the Kunlun fault: Implications for seismic behavior and large-scale tectonics: Geophysical Research Letters, v. 27, p. 2353–2356, doi:10.1029/1999GL011292.

Van der Woerd, J., Xu, X., Haibing, L.P., Tapponnier, P., Meyer, B., Ryerson, F.J., Meriaux, A.-S., and Xu, Z., 2001, Rapid active thrusting along the northwestern range front of the Tanghe Nan Shan (western Gansu, China): Journal of Geophysical Research–Solid Earth, v. 106, no. B12, p. 30,475–30,504, doi:10.1029/2001JB000583.

Van der Woerd, J., Tapponnier, P., Ryerson, F.J., Meriaux, A.-S., Meyer, B., Gaudemer, Y., Finkel, R.C., Caffee, M.W., Zhao, G., and Xu, Z., 2002, Uniform postglacial slip-rate along the central 600 km of the Kunlun fault (Tibet), from $^{26}$Al, $^{10}$Be, and $^{14}$C dating of riser offsets, and climatic origin of the regional morphology: Geophysical Journal International, v. 148, no. 3, p. 356–388, doi:10.1046/j.1365-246x.2002.01556.x.

Vergne, J., Wittlinger, G., Hui, Q., Tapponnier, P., Poupinet, G., Mei, J., Herquel, G., and Paul, A., 2002, Seismic evidence for stepwise thickening of crust across the NE Tibetan Plateau: Earth and Planetary Science Letters, v. 203, p. 25–33, doi:10.1016/S0012-821X(02)00853-1.

Vermeesch, P., 2009, RadialPlotter: A Java application for fission track, luminescence and other radial plots: Radiation Measurements, v. 44, p. 409–410, doi:10.1016/j.radmeas.2009.05.003.

Wang, C., Gao, R., Yin, A., Wang, H., Zhang, Y., Guo, T., Li, Q., and Li, Y., 2011, A mid-crustal strain-transfer model for continental deformation: A new perspective from high-resolution deep seismic-reflection profiling across NE Tibet: Earth and Planetary Science Letters, v. 306, no. 3, p. 279–288, doi:10.1016/j.epsl.2011.04.010.

Wang, E., Xu, F.-Y., Zhou, J.-X., Wan, J., and Burchfiel, B.C., 2006, Eastward migration of the Qaidam Basin and its implications for Cenozoic evolution of the Altyn Tagh fault and associated river systems: Geological Society of America Bulletin, v. 118, no. 3–4, p. 349–365, doi:10.1130/B25778.1.

Wang, E., Kirby, E., Furlong, K.P., van Soest, M., Xu, G., Shi, X., and Hodges, K.V., 2012, Two-phase growth of high topography in eastern Tibet during the Cenozoic: Nature Geoscience, v. 5, no. 9, p. 640–645, doi:10.1038/ngeo1538.

Wei, W.T., Unsworth, M., Jones, A., Booker, J., Tan, H., Nelson, D., Chen, L., Li, S., Solon, K., Bedrosian, P., Jin, S., Deng, M., Ledo, J., Kay, D., and Roberts, B., 2001, Detection of widespread fluids in the Tibetan crust by magnetotelluric studies: Science, v. 292, p. 716–719, doi:10.1126/science.1010580.

Woodward, N.B., Boyer, S.E., and Suppe, J., 1989, Balanced Geological Cross-Sections: An Essential Technique in Geological Research and Exploration: Washington, D.C., American Geophysical Union, Short Course Geology Series, v. 6, 132 p., doi:10.1029/SC006.

Xiao, W., Windley, B.F., Yong, Y., Yan, Z., Yuan, C., Liu, C., and Li, J., 2009, Early Paleozoic to Devonian multiple-accretionary model for the Qilian Shan, NW China: Journal of Asian Earth Sciences, v. 35, p. 323–333, doi:10.1016/j.jseaes.2008.10.001.

Yakovlev, P.V., and Clark, M.K., 2014, Conservation and redistribution of crust during the Indo-Asian collision: Tectonics, v. 33, p. 1016–1027, doi:10.1002/2013TC003440.

Yang, Y., Ritzwoller, M.H., Zheng, Y., Shen, W., Levshin, A.L., and Xie, Z., 2012, A synoptic view of the distribution and connectivity of the mid-crustal low velocity zone beneath Tibet: Journal of Geophysical Research, v. 117, B04303, doi:10.1029/2011JB008810.

Yin, A., and Harrison, T.M., 2000, Geological evolution of the Himalayan-Tibetan orogen: Annual Review of Earth and Planetary Sciences, v. 28, p. 211–280, doi:10.1146/annurev.earth.28.1.211.

Yin, A., Dang, Y.-Q., Zhang, M., McRivette, M.W., Burgess, W.P., and Chen, X.-H., 2007a, Cenozoic tectonic evolution of Qaidam Basin and its surrounding regions (part 2): Wedge tectonics in southern Qaidam Basin and the Eastern Kunlun Range, *in* Sears, J.W., Harms, T.A., and Evenchick, C.A., eds., Whence the Mountains? Inquiries into the Evolution of Orogenic Systems: A Volume in Honor of Raymond A. Price: Geological Society of America Special Paper 433, p. 369–390, doi:10.1130/2007.2433(18).

Yin, A., Manning, C.E., Lovera, O., Menold, C.A., Chen, X., and Gehrels, G.E., 2007b, Early Paleozoic tectonic and thermomechanical evolution of ultrahigh-pressure (UHP) metamorphic rocks in the northern Tibetan Plateau, northwest China: International Geology Review, v. 49, p. 681–716, doi:10.2747/0020-6814.49.8.681.

Yin, A., Dang, Y.-Q., Wang, L.-C., Jiang, W.-M., Zhou, S.-P., Chen, X.-H., Gehrels, G.E., and McRivette, M.W., 2008a, Cenozoic tectonic evolution of Qaidam Basin and its surrounding regions (Part 1): The southern Qilian Shan–Nan Shan thrust belt and northern Qaidam Basin: Geological Society of America Bulletin, v. 120, no. 7–8, p. 813–846, doi:10.1130/B26180.1.

Yin, A., Dang, Y.-Q., Zhang, M., Chen, M., Chen, X.-H., and McRivette, M.W., 2008b, Cenozoic tectonic evolution of the Qaidam Basin and its surrounding regions (Part 3): Structural geology, sedimentation, and regional tectonic reconstruction: Geological Society of America Bulletin, v. 120, no. 7–8, p. 847–876, doi:10.1130/B26232.1.

Yuan, D., Champagnac, J.D., Ge, W.-P., Molnar, P., Zhang, P.-Z., Zheng, W.-J., Zhang, H.-P., and Liu, X.-W., 2011, Late Quaternary right-lateral slip rates of faults adjacent to the lake Qinghai, northeastern margin of the Tibetan Plateau: Geological Society of America Bulletin, v. 123, no. 9–10, p. 2016–2030, doi:10.1130/B30315.1.

Yuan, D.Y., Ge, W.P., Chen, Z.W., Li, C.Y., Wang, Z.C., Zhang, H.P., Zhang, P.Z., Zheng, D.W., Zheng, W.J., Craddock, W.H., Dayem, K.E., Duvall, A.R., Hough, B.G., Lease, R.O., Champagnac, J.D., Burbank, D.W., Clark, M.K., Farley, K.A., Garzione, C.N., Kirby, E., Molnar, P., and Roe, G.H., 2013, The growth of northeastern Tibet and its relevance to large-scale continental geodynamics: A review of recent studies: Tectonics, v. 32, p. 1358–1370, doi:10.1002/tect.20081.

Zhang, H.-P., Craddock, W.H., Lease, R.O., Wang, W.-T., Yuan, D.-Y., Zhang, P.-Z., Molnar, P., Zheng, D.-W., and Zheng, W.-J., 2012, Magnetostratigraphy of the Neogene Chaka Basin and its implications for mountain building processes in the north-eastern Tibetan Plateau: Basin Research, v. 24, no. 1, p. 31–50, doi:10.1111/j.1365-2117.2011.00512.x.

Zhang, L.-Y., Ding, L., Pullen, A., Xu, Q., Lu, D.-L., Cai, F.-L., Yue, Y.-H., Lai, Q.-Z., Shi, R.-D., Ducea, M.N., Kapp, P., and Chapman, A., 2014, Age and geochemistry of western Hoh-Xil-Songpan-Ganzi granitoids, northern Tibet: Implications for Mesozoic closure of the Paleo-Tethys ocean: Lithos, v. 190–191, p. 328–348, doi:10.1016/j.lithos.2013.12.019.

Zhang, P.Z., Burchfiel, B.C., Molnar, P., Zhang, W., Jiao, D., Deng, Q., Wang, Y., Royden, L.H., and Song, F., 1991, Amount and style of late Cenozoic deformation in the Liupan Shan area, Ningxia Autonomous Region, China: Tectonics, v. 10, no. 6, p. 1111–1129, doi:10.1029/90TC02686.

Zhang, P.Z., Shen, Z., Wang, M., Gan, W., Burgmann, R., Molnar, P., Wang, Q., Niu, Z., Sun, J., Wu, J., Sun, H., and Xinzhao, Y., 2004, Continuous deformation of the Tibetan Plateau from global positioning system data: Geology, v. 32, no. 9, p. 809–812, doi:10.1130/G20554.1.

Zhang, Z., Klemperer, S., Bai, Z., Chen, Y., and Teng, J., 2011, Crustal structure of the Paleozoic Kunlun orogeny from an active-source seismic profile between Moba and Guide in east Tibet, China: Gondwana Research, v. 19, no. 4, p. 994–1007, doi:10.1016/j.gr.2010.09.008.

Zheng, D., Zhang, P., Wan, J., Yuan, D., Li, C., Yin, G., Zhang, G., Wang, Z., Min, W., and Chen, J., 2006, Rapid exhumation at ~8 Ma on the Liupan Shan thrust fault from apatite fission-track thermochronology: Implications for growth of the northeastern Tibetan Plateau margin: Earth and Planetary Science Letters, v. 248, no. 1–2, p. 198–208, doi:10.1016/j.epsl.2006.05.023.

Zheng, D., Clark, M.K., Zhang, P., Zheng, W.J., and Farley, K.A., 2010, Erosion, fault initiation and topographic growth of the North Qilian Shan (northern Tibetan Plateau): Geosphere, v. 6, no. 6, p. 937–941, doi:10.1130/GES00523.1.

Zheng, S.H., Wu, W.Y., Li, Y., and Wang, G.D., 1985, Late Cenozoic mammalian faunas of Guide and Gonghe basins, Qinghai Province: Vertabrata PalAsiatica, v. 23, no. 2, p. 89–134.

Zheng, W.-J., Zhang, H.-P., Zhang, P.-Z., Molnar, P., Liu, X.-W., and Yuan, D.-Y., 2013, Late Quaternary slip rates of the thrust faults in the western Hexi Corridor (northern Qilian Shan, China) and their implications for northeastward growth of the Tibetan Plateau: Geosphere, v. 9, no. 2, p. 342–354, doi:10.1130/GES00775.1.

Zhu, L.P., and Helmberger, I.V., 1998, Moho offset across the northern margin of the Tibetan Plateau: Science, v. 281, p. 1170–1172, doi:10.1126/science.281.5380.1170.